

## Understanding the Excited State Behavior of Cyclometalated Bis(tridentate)ruthenium(II) Complexes: A Combined Experimental and Theoretical Study

Christoph Kreitner,<sup>†,‡</sup> Elisa Erdmann,<sup>§</sup> Wolfram W. Seidel,<sup>§</sup> and Katja Heinze<sup>\*,†</sup>

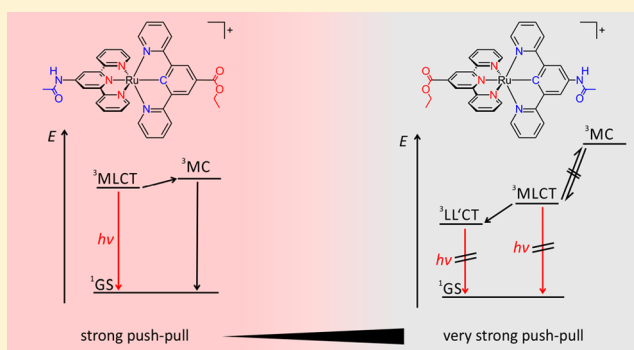
<sup>†</sup>Institute of Inorganic and Analytical Chemistry, Johannes Gutenberg-University of Mainz, Duesbergweg 10-14, 55128 Mainz, Germany

<sup>‡</sup>Graduate School Materials Science in Mainz, Staudingerweg 9, 55128 Mainz, Germany

<sup>§</sup>Institute of Chemistry, University of Rostock, Albert-Einstein-Straße 3a, 18059 Rostock, Germany

### Supporting Information

**ABSTRACT:** The synthesis and characterization of the donor–acceptor substituted cyclometalated ruthenium(II) polypyridine complex isomers [Ru(dpb-NHCOMe)(tpy-COOEt)](PF<sub>6</sub>) **1**(PF<sub>6</sub>) and [Ru(dpb-COOEt)(tpy-NHCOMe)](PF<sub>6</sub>) **2**(PF<sub>6</sub>) (dpbH = 1,3-dipyridin-2-ylbenzene, tpy = 2,2';6,2''-terpyridine) with inverted functional group pattern are described. A combination of resonance Raman spectroscopic and computational techniques shows that all intense visible range absorption bands arise from mixed Ru → tpy/Ru → dpb metal-to-ligand charge transfer (MLCT) excitations. **2**(PF<sub>6</sub>) is weakly phosphorescent at room temperature in fluid solution and strongly emissive at 77 K in solid butyronitrile matrix, which is typical for ruthenium(II) polypyridine complexes. Density functional theory calculations revealed that the weak emission of **2**(PF<sub>6</sub>) arises from a <sup>3</sup>MLCT state that is efficiently thermally depopulated via metal-centered (<sup>3</sup>MC) excited states. The activation barrier for the deactivation process was estimated experimentally from variable-temperature emission spectroscopic measurements as 11 kJ mol<sup>−1</sup>. In contrast, **1**(PF<sub>6</sub>) is nonemissive at room temperature in fluid solution and at 77 K in solid butyronitrile matrix. Examination of the electronic excited states of **1**(PF<sub>6</sub>) revealed a ligand-to-ligand charge-transfer (<sup>3</sup>LL'CT) as lowest-energy triplet state due to the very strong push–pull effect across the metal center. Because of the orthogonality of the participating ligands, emission from the <sup>3</sup>LL'CT is symmetry-forbidden. Hence, in this type of complex a stronger push–pull effect does not increase the phosphorescence quantum yields but completely quenches the emission.



## INTRODUCTION

Polypyridine complexes of ruthenium have been studied extensively in the last 50 years.<sup>1</sup> Especially, the photophysics and photochemistry of their prototype [Ru(bipy)<sub>3</sub>]<sup>2+</sup> (bipy = 2,2'-bipyridine) are well understood.<sup>2–5</sup> The visible range of the absorption spectrum is dominated by an intense metal-to-ligand charge transfer (MLCT) absorption from ruthenium d-orbitals into the low-lying antibonding  $\pi^*$ -orbitals of the bipy ligands<sup>3,6</sup> with an absorption maximum at 452 nm and an extinction coefficient of 14 600 M<sup>−1</sup> cm<sup>−1</sup>.<sup>4</sup> The UV region is dominated by  $\pi$ – $\pi^*$  transitions within the aromatic ligands.<sup>4</sup> Following Kasha's rule<sup>7</sup> rapid vibrational relaxation and internal conversion occur upon optical excitation populating the lowest-energy <sup>1</sup>MLCT state. From this state nearly quantitative intersystem crossing (ISC)<sup>8,9</sup> onto the triplet hypersurface occurs, which leads to population of the lowest-energy <sup>3</sup>MLCT state.<sup>10</sup> This state is highly phosphorescent<sup>10</sup> at room temperature ( $\lambda_{\text{em}} = 621$  nm,  $\phi = 0.095$  in acetonitrile)<sup>11</sup> and

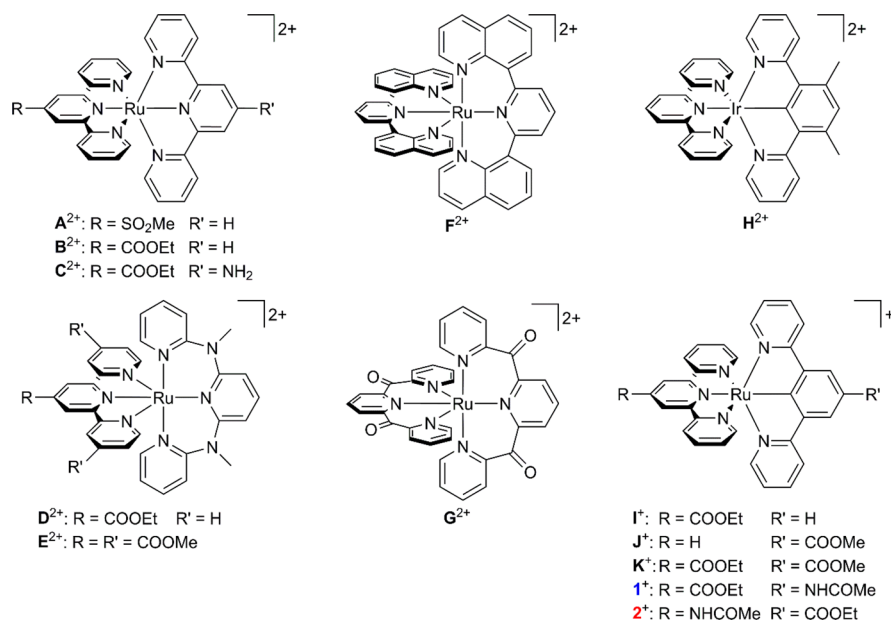
has a long excited-state lifetime of 855 ns (in acetonitrile) due to the spin-forbidden character of the luminescence.<sup>5</sup>

A qualitatively similar picture of the excited-state mechanisms is gained for the meridionally coordinated<sup>12</sup> tridentate analogue of [Ru(bipy)<sub>3</sub>]<sup>2+</sup>, namely, [Ru(tpy)<sub>2</sub>]<sup>2+</sup> (tpy = 2,2';6',2''-terpyridine). MLCT absorption occurs at 474 nm slightly bathochromically and hyperchromically shifted ( $\epsilon = 16\,100$  M<sup>−1</sup> cm<sup>−1</sup>)<sup>13</sup> due to the larger accepting  $\pi^*$ -orbitals of the terpyridine ligands. Upon ISC again <sup>3</sup>MLCT states are populated.<sup>14,15</sup> In contrast to the bipy counterpart an efficient deactivation pathway is available for this emissive <sup>3</sup>MLCT state: because of the smaller N–Ru–N bite angles in this tpy complex compared to the parent bipy complex the orbital overlap of the pyridine nitrogen lone pairs with the ruthenium d orbitals of the  $e_g$  set (in idealized  $O_h$  symmetry) is lowered. The loss in ligand-field splitting shifts d–d excited states (<sup>3</sup>MC states, MC

Received: May 27, 2015

Published: August 6, 2015



Scheme 1. Bis(tridentate)ruthenium(II) and Iridium(III) Polypyridine Complexes<sup>a</sup>

<sup>a</sup>By Constable ( $A^{2+}$ ),<sup>15</sup> van Koten ( $B^{2+}$ ,  $I^+$ ,  $J^+$ ,  $K^+$ ),<sup>20</sup> Heinze ( $C^{2+}$ ,  $D^{2+}$ ,  $E^{2+}$ ),<sup>21–23</sup> Hammarström ( $F^{2+}$ ),<sup>24</sup> Ruben ( $G^{2+}$ ),<sup>25</sup> Williams ( $H^{2+}$ ),<sup>26</sup> and from this work ( $L^+$  and  $M^+$ ).

= metal-centered) into the energy regime of the <sup>3</sup>MLCT states. These MC states are thermally populated at room temperature and lead to an efficient emission quenching in  $[Ru(tpy)_2]^{2+}$  ( $\lambda_{em} = 629$  nm,  $\phi < 1 \times 10^{-5}$ ).<sup>16</sup> At 77 K, the available thermal energy does not suffice to overcome the activation barrier for population of the <sup>3</sup>MC states, and an intense emission is regained ( $\phi = 0.48$ ).<sup>13</sup>

Just as this undesirable side effect also the major advantage of bis(terpyridine)ruthenium(II) complexes over their bipyridine analogues arises from their coordination geometry. The  $C_{2v}$  symmetry of the core structure of this complex<sup>12</sup> prevents the formation of diastereomers even when heteroleptic complexes bearing ligands with different functional groups are formed. Syntheses of similarly substituted bipyridine complexes usually give mixtures of diastereomers that require elaborate methods to be purified<sup>17</sup> or to be circumvented.<sup>18,19</sup>

Several successful approaches improve the emissive behavior of bis(tridentate)ruthenium complexes by influencing the energies of the relevant excited states.<sup>27</sup> Introducing  $\pi$ -accepting functional groups ( $-SO_2R$ ,  $-COOR$ , Scheme 1,  $A^{2+}$ ,  $B^{2+}$ ) in the ligand backbone (typically in 4'-position) lowers the energy of the <sup>3</sup>MLCT states while leaving the energy of the <sup>3</sup>MC states unaltered. This hinders the thermal deactivation process to some extent and increases both excited-state lifetimes and quantum yields of such compounds ( $\phi \approx 1-5 \times 10^{-4}$ ).<sup>15,28</sup> Alternatively, introducing  $\sigma$ -donating functional groups in the ligand's periphery directly influences the energy of the <sup>3</sup>MC states.<sup>15</sup> They are shifted to higher energies with respect to the <sup>3</sup>MLCT states again hampering thermal depopulation of the latter. Combining both approaches yields excited-state lifetimes of up to 50 ns (Scheme 1,  $A^{2+}$ )<sup>15</sup> and quantum yields of up to 0.003 (Scheme 1,  $C^{2+}$ )<sup>21,29</sup> but always at the cost of a lowered excited-state energy.<sup>27</sup>

The <sup>3</sup>MC states are even more efficiently shifted to higher energies by widening the N–Ru–N bite angles. This is achieved upon introduction of N–CH<sub>3</sub> in between the pyridine rings of the terpyridine ligand (*N,N'*-dimethyl-*N,N'*-dipyridine-

2-ylpyridine-2,6-diamine, ddpd).<sup>22</sup> The increased  $\sigma$ -donor strength of ddpd compared to tpy sufficiently separates the <sup>3</sup>MC states in the heteroleptic complex  $[Ru(ddpd)(tpy-COOEt)]^{2+}$   $D^{2+}$  (Scheme 1) from the <sup>3</sup>MLCT states to allow  $[Ru(ddpd)(tpy)]^{2+}$  to be emissive ( $\phi = 0.0045$ ) despite its much lower emission energy ( $\lambda_{em} = 729$  nm).<sup>22,23</sup> Gradually tuning the vertical <sup>3</sup>MLCT  $\rightarrow$  <sup>1</sup>GS transition energy within a series of structurally similar  $[Ru(ddpd)(tpy)]^{2+}$  complexes by variation of appended functional groups decreases the emission quantum yield with decreasing emission energy following the energy gap law as pointed out by Meyer and co-workers.<sup>30–32</sup> Similarly, Hammarström and co-workers used di(quinolin-8-yl)pyridine (dqp) as tridentate ligand forming six-membered chelate rings with ruthenium as metal center.<sup>24,33</sup> The homoleptic complex  $[Ru(dqp)_2]^{2+}$   $F^{2+}$  (Scheme 1) is phosphorescent at room temperature ( $\phi = 0.02$ ) with a remarkably long excited-state lifetime of 3.0  $\mu$ s. Ruben and co-workers employed the carbonyl analogue of the ddpd ligand, 2,6-di(2-carboxypyridyl)pyridine (dcp) as chelating ligand with N–Ru–N bite angles of 90°. The homoleptic complex  $[Ru(dcp)_2]^{2+}$   $G^{2+}$  (Scheme 1) exhibits an extraordinary high room-temperature emission quantum yield of 0.30 with a long excited-state lifetime of 3.3  $\mu$ s.<sup>25</sup>

Cyclometalation<sup>34,35</sup> (i.e., isoelectronic substitution of a nitrogen atom for a carbanion in the coordination sphere around the metal) is discussed as another option for raising the <sup>3</sup>MC states since the strong  $\sigma$ -donating effect of the anionic carbon greatly increases the ligand field splitting.<sup>20</sup> While for iridium(III) a large variety of highly phosphorescent cyclometalated complexes are known,<sup>36–39</sup> most cyclometalated ruthenium(II) complexes are barely emissive at room temperature.<sup>40–42</sup> For tris(bidentate)iridium(III) complexes with cyclometalating ligands of the type  $[Ir(bipy)_n(ppy)_{3-n}]^{3+}$  ( $n = 1, 2$ ; ppyH = 2-phenylpyridine) the excited-state mechanisms that are responsible for the efficient luminescence are well-understood.<sup>43</sup> The emissive excited state of Ir<sup>III</sup> complexes is a linear combination of a mixed <sup>3</sup>MLCT/<sup>3</sup>LL'CT state (LL'CT =

ligand-to-ligand charge-transfer state) and an energetically very similar ligand-centered ( $^3\text{LC}$ ) excited state due to the very high ligand field splitting of  $\text{Ir}^{\text{III}}$  combined with the ppy ligands. This state is well-separated from other states so that emission becomes very efficient.<sup>26,44–46</sup> Since most cyclometalated ruthenium complexes are essentially nonemissive at room temperature in solution it is much more difficult to obtain a profound understanding of the excited-state mechanisms in these systems. Berlinguette and co-workers showed that the energy gap law is obeyed in complexes of type  $[\text{Ru}(\text{bipy})_2(\text{ppy})]^+$  demonstrating that direct ISC onto the singlet hypersurface followed by vibrational cooling is the dominant deactivation pathway.<sup>41,42</sup>

Van Koten and co-worker recently discussed  $[\text{Ru}(\text{tpy-R})(\text{pbpy-R}')^+]$  ( $\text{pbpyH}$  = 6-phenyl-2,2'-bipyridine) and  $[\text{Ru}(\text{tpy-R})(\text{dpb-R}')^+]$  ( $\text{dpbH}$  = 2,6-di(pyrid-2'-yl)benzene) complexes and their application in dye-sensitized solar cells.<sup>20,47,48</sup> Electron-accepting anchor groups (COOR) were appended at either one of the two ligands or at both resulting in a series of weakly or nonemissive tridentate complexes (Scheme 1,  $\text{I}^+$ ,  $\text{J}^+$ , and  $\text{K}^+$ ). A structurally similar weakly emitting iridium(III) complex (Scheme 1,  $\text{H}^{2+}$ ) was synthesized by Williams and co-workers.<sup>26</sup> Despite the fact that the energy gap law is obeyed within these complex series luminescence quenching is discussed to arise from thermal depopulation of the very low-lying  $^3\text{MLCT}$  states via  $^3\text{MC}$  states. However, the latter should be high in energy due to the strong  $\sigma$ -donor strength of the cyclometalating ligand.<sup>20</sup> This apparent discrepancy will be addressed in this paper.

In this study we present an extension of our previous work on tridentate polypyridine ruthenium complexes bearing both electron-donating amino and electron-withdrawing carboxylic acid functionalities (such as  $\text{A}^{2+}$ , Scheme 1)<sup>21,27</sup> into the field of cyclometalated complexes and elucidate the excited-state deactivation mechanisms of these complexes in detail. In the isomeric  $[\text{Ru}(\text{dpb-R}')(\text{tpy-R})]^+$  complexes ( $\text{I}^+$ :  $\text{R} = \text{COOEt}$ ,  $\text{R}' = \text{NHCOMe}$ ;  $\text{2}^+$ :  $\text{R} = \text{NHCOMe}$ ,  $\text{R}' = \text{COOEt}$ ) the position of the functional groups with respect to the site of cyclometalation should have a strong impact on their electronic structure and excited-state ordering. The ground- and excited-state electronic structures as well as excited-state dynamics are elucidated by a combination of UV-vis, electron paramagnetic resonance (EPR), resonance Raman (rR), and emission spectroscopies and theoretical techniques to provide a better understanding of the unexplained low-emission efficiencies in cyclometalated bis(tridentate)ruthenium(II) complexes.

## EXPERIMENTAL SECTION

**General Procedures.** Chemicals were obtained from commercial suppliers and used without further purification. Air- or moisture-sensitive reactions were performed in dried glassware in an inert gas atmosphere (argon, quality 4.6). Acetonitrile and dichloromethane were refluxed over  $\text{CaH}_2$  and distilled under argon prior to use. Toluene and xylenes were refluxed over sodium and distilled prior to use. Palladium precatalyst  $[\text{Pd}]_2$ <sup>49</sup> and the ligand precursors 1-bromo-3,5-dipyridin-2-ylbenzene **LA**,<sup>50</sup> 4'-chloro-2,2':6',2''-terpyridine **LB**,<sup>51</sup> 4'-amino-2,2':6',2''-terpyridine **LC**,<sup>52</sup> and ethyl 3,5-dibromobenzoate **LD**<sup>53</sup> were synthesized following literature-known procedures. UV-vis spectra were recorded on a Varian Cary 5000 spectrometer in 1 cm cuvettes. Emission spectra were recorded on a Varian Cary Eclipse spectrometer. Quantum yields were determined by comparing the areas under the emission spectra on an energy scale recorded for solutions of the samples and a reference with matching absorbances ( $\phi([\text{Ru}(\text{bipy})_3]\text{Cl}_2) = 0.094$  in deaerated  $\text{CH}_3\text{CN}$ ).<sup>11</sup> Experimental

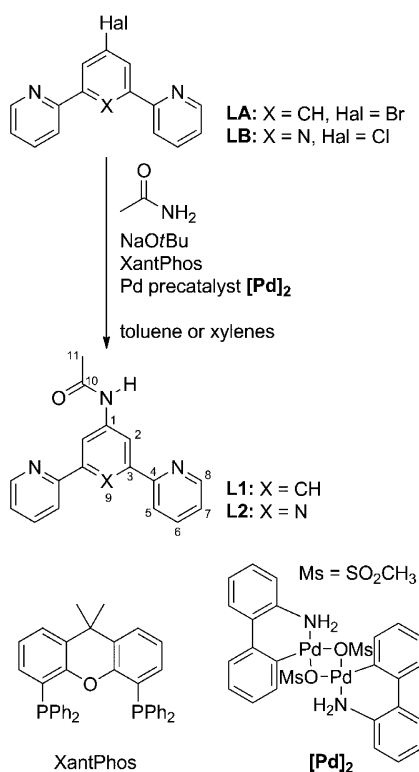
uncertainty is estimated to be 15%.  $\text{FD}^+$  mass spectra were recorded on a  $\text{FD}$  Finnigan MAT95 spectrometer. Electrospray ionization ( $\text{ESI}^+$ ) and high-resolution  $\text{ESI}^+$  mass spectra were recorded on a Micromass QToF Ultima API mass spectrometer with analyte solutions in acetonitrile. Elemental analyses were performed by the micro-analytical laboratory of the chemical institutes of the University of Mainz. NMR spectra were obtained with a Bruker Avance II 400 spectrometer at 400.31 ( $^1\text{H}$ ) and 100.66 ( $^{13}\text{C}$ ) at 25 °C. Chemical shifts  $\delta$  [parts per million] are reported with respect to residual solvent signals as internal standards ( $^1\text{H}$ ,  $^{13}\text{C}$ ):  $\text{CD}_3\text{CN}$   $\delta(^1\text{H}) = 1.94$  ppm,  $\delta(^{13}\text{C}) = 1.32$  and 118.26 ppm.<sup>54</sup> Electrochemical experiments were performed with a BioLogic SP-50 voltammetric analyzer at a sample concentration of  $1 \times 10^{-3}$  M using platinum wire working and counter electrodes and a 0.01 M  $\text{Ag}/\text{AgNO}_3$  reference electrode. Measurements were performed at a scan rate of 100  $\text{mV s}^{-1}$  for cyclic voltammetry experiments and at 10  $\text{mV s}^{-1}$  for square-wave voltammetry experiments using 0.1 M  $[\text{Bu}_4\text{N}][\text{PF}_6]$  as supporting electrolyte in acetonitrile. Potentials are given relative to the ferrocene/ferrocenium couple (0.40 V vs standard calomel electrode (SCE),  $E_{1/2} = 0.90 \pm 5$  mV under the given conditions).<sup>55</sup> EPR spectra were recorded on a Miniscope MS 300 X-band CW spectrometer (Magnettech GmbH, Germany). Values of  $g$  are referenced against  $\text{Mn}^{2+}$  in ZnS as external standard ( $g = 2.118, 2.066, 2.027, 1.986, 1.946$ ). Simulations were performed with the EasySpin program package.<sup>56</sup> A Horiba LabRAM HR Raman microscope was used for rR measurements with an object lens (10 $\times$  NA 0.25) from Olympus. Samples were optically excited with a red laser (633 nm, 17 mW, HeNe-laser), green laser (532 nm, 50 mW, air-cooled frequency-doubled Nd:YAG-solid state laser), or blue laser (473 nm, 20 mW, air-cooled solid-state laser). Samples were measured in acetonitrile (Chemsolute, for HPLC) solution in capillary tubes (80  $\times$  1.5 mm, Marienfeld-Superior).

Density functional theory (DFT) calculations were performed using the ORCA program package (version 3.0.2).<sup>57</sup> Tight convergence criteria were chosen for all calculations (keywords TightSCF and TightOpt, convergence criteria for the SCF part: energy change  $1.0 \times 10^{-8}$   $E_h$ ,  $1 - E_i$  energy change  $1.0 \times 10^{-5}$   $E_h$ , orbital gradient  $1.0 \times 10^{-5}$ , orbital rotation angle  $1.0 \times 10^{-5}$ , DIIS error  $5.0 \times 10^{-7}$ ; for geometry optimizations: energy change:  $1.0 \times 10^{-6}$   $E_h$ , maximum gradient  $1.0 \times 10^{-4}$   $E_h/\text{bohr}$ , root-mean-square (RMS) gradient  $3.0 \times 10^{-5}$   $E_h/\text{bohr}$ , maximum displacement  $1.0 \times 10^{-3}$  bohr, RMS displacement  $6.0 \times 10^{-4}$  bohr). All calculations employ the resolution of identity (Split-RI-J) approach for the coulomb term in combination with the chain-of-spheres approximation for the exchange term (COSX) where Hartree-Fock exchange is required.<sup>58,59</sup> Geometry optimizations were performed using the GGA functional PBE<sup>60,61</sup> in combination with Ahlrichs' split-valence double- $\xi$  basis set def2-SV(P) for all atoms except ruthenium, which comprises polarization functions for all non-hydrogen atoms.<sup>62,63</sup> For ruthenium a Stuttgart-Dresden effective core potential (ECP, def2-SD) was combined with Ahlrichs' def2-TZVP basis set for the valence electrons.<sup>64,65</sup> To account for solvent effects a conductor-like screening model (COSMO) modeling acetonitrile was used in all calculations except for excited-state gradients.<sup>66</sup> This proved to be particularly important for time-dependent DFT calculations (TD-DFT) where gas phase calculations lead to a substantial underestimation of excitation energies.<sup>67</sup> The optimized geometries were confirmed to be local minima on the respective potential energy surface by subsequent numerical frequency analysis ( $N_{\text{imag}} = 0$ ).

Calculation of EPR parameters and TD-DFT calculations were performed based on the PBE/def2-SV(P)/ECP(def2-TZVP) optimized geometry of the respective complex employing the triple- $\xi$  basis set def2-TVZP and several functionals with varying amounts of HF exchange:<sup>68</sup> PBE (0%), TPSSH (10%),<sup>69</sup> B3LYP (20%),<sup>70</sup> PBE0 (25%),<sup>71</sup> and CAM-B3LYP (19–65%).<sup>72</sup> The Douglas-Kroll-Hess (DKH) relativistic approximation<sup>73–76</sup> was used to describe relativistic effects in these calculations. The DKH keyword in ORCA automatically invokes adjusted basis sets (TZV\_DKH).<sup>77</sup> At least 50 vertical transitions were calculated in TD-DFT calculations. The electron  $g$  value and hyperfine coupling constants of the unpaired electron to the



ruthenium atom and all atoms coordinated to ruthenium were determined in EPR calculations. On the basis of the optimized <sup>1</sup>GS molecular geometries and the associated Hessian matrices excited-state gradients were calculated for the lowest 10 excitations at the B3LYP/def2-TZVP/DKH level of theory to generate excited-state displacements for the rR spectra simulation. The advanced spectra analysis tool provided with the ORCA program package (orca\_asa)<sup>78,79</sup> was employed to fit the absorption spectra of **1**(PF<sub>6</sub>) and **2**(PF<sub>6</sub>) and to simulate rR spectra. The Gibbs free energy was used to compare relative energies of the different triplet states of the complexes under study. Explicit counterions and/or solvent molecules were not taken into account in all cases. To reduce the computational cost methyl instead of ethyl groups were used throughout all calculations at the ester moiety.

Scheme 2<sup>a</sup>

<sup>a</sup>Buchwald–Hartwig amination of 1-bromo-3,5-di(pyridin-2-yl)-benzene **LA** and 4'-chloro-2,2':6',2''-terpyridine **LB** with acetamide yielding *N*-acetyl-3,5-di(pyridin-2-yl)aniline **L1** and *N*-acetyl-4'-amino-2,2':6',2''-terpyridine **L2**. Atom numbering for NMR assignment is included.

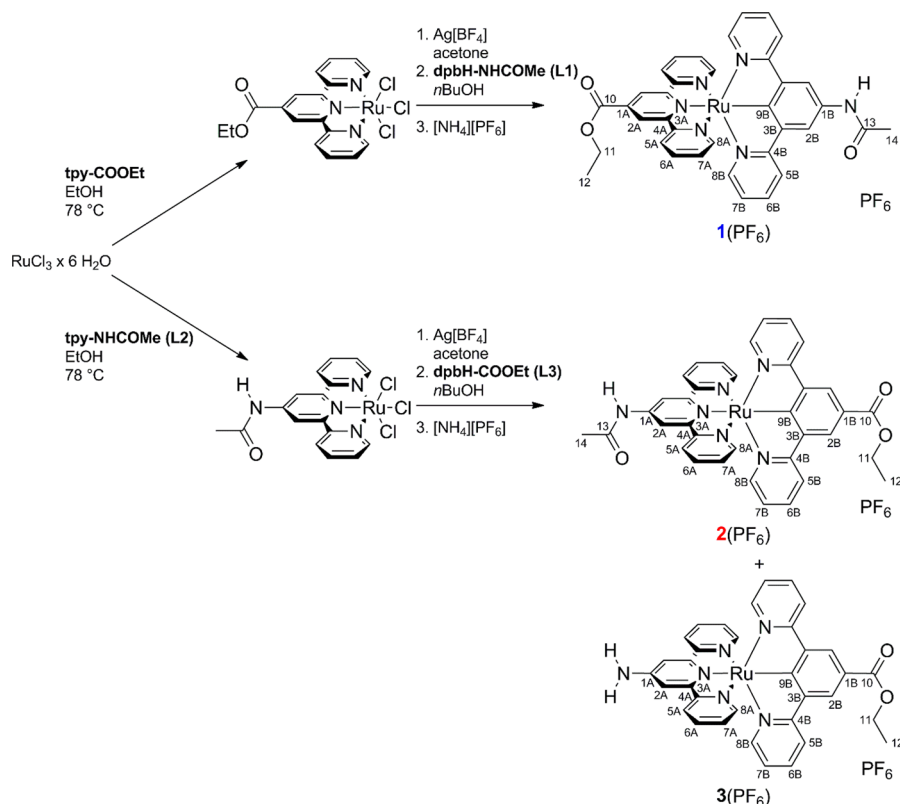
**Synthesis of *N*-Acetyl-3,5-di(pyridin-2-yl)aniline L1.** 4,5-Bis-(diphenylphosphino)-9,9-dimethylxanthene (XantPhos, 64 mg, 111 μL, 3 mol %) and Pd precatalyst [Pd]<sub>2</sub> (14 mg, 19 μmol, 1.1 mol % based on Pd) were dissolved under argon in 15 mL of abs. toluene and left to stand. After 10 min 1-bromo-3,5-di(pyridin-2-yl)benzene **LA** (1.15 g, 3.70 mmol, 1 equiv), acetamide (273 mg, 4.62 mmol, 1.25 equiv), and sodium *tert*-butanolate (444 mg, 4.62 mmol, 1.25 equiv), dissolved in 15 mL of abs. toluene, were added, and the mixture was heated to reflux for 8 h. After the mixture cooled to room temperature, the solvent was removed under reduced pressure, and the remaining solid was dissolved in concentrated hydrochloric acid (20 mL), water (20 mL), and dichloromethane (50 mL). The phases were separated, and the aqueous phase was extracted twice with dichloromethane (2 × 50 mL). The aqueous phase was neutralized with dilute aqueous sodium hydroxide solution (pH = 9) followed by extraction with dichloromethane (3 × 50 mL). The organic fractions of the second extraction were dried over magnesium sulfate, and the solvent was

removed under reduced pressure to give 0.95 g of crude *N*-acetyl-3,5-di(pyridin-2-yl)aniline. After column chromatography on neutral Alox (Brockmann II, 3% water (w/w), solvent ethyl acetate) the product was obtained as colorless powder. Yield: 848 mg (2.90 mmol, 78%). Anal. Calcd C<sub>18</sub>H<sub>15</sub>N<sub>3</sub>O (289.33): C, 74.72; H, 5.23; N, 14.52. Found: C, 74.93; H, 4.98; N, 14.39%. MS(FD<sup>+</sup>): *m/z* (%) = 289.2 (100) [M]<sup>+</sup>, 579.4 (2) [2M+H]<sup>+</sup>. <sup>1</sup>H NMR (CD<sub>2</sub>Cl<sub>2</sub>): δ [ppm] = 8.67 (ddd, <sup>3</sup>J<sub>HH</sub> = 5 Hz, <sup>4</sup>J<sub>HH</sub> = 2 Hz, 1 Hz, 2H, H<sup>8</sup>), 8.38 (t, <sup>4</sup>J<sub>HH</sub> = 1 Hz, 1H, H<sup>9</sup>) 8.27 (d, <sup>4</sup>J<sub>HH</sub> = 1 Hz, 2H, H<sup>2</sup>), 8.25 (s, 1H, NH), 7.79 (ddd, <sup>3</sup>J<sub>HH</sub> = 8 Hz, <sup>4</sup>J<sub>HH</sub> = 1 Hz, 2H, H<sup>5</sup>), 7.74 (vtd, <sup>3</sup>J<sub>HH</sub> = 8, <sup>4</sup>J<sub>HH</sub> = 2 Hz, 2H, H<sup>6</sup>), 7.24 (ddd, <sup>3</sup>J<sub>HH</sub> = 8 Hz, 5 Hz, <sup>4</sup>J<sub>HH</sub> = 1.2 Hz, 2H, H<sup>7</sup>), 2.12 (s, 3H CH<sub>3</sub>). <sup>13</sup>C{<sup>1</sup>H} NMR (CD<sub>2</sub>Cl<sub>2</sub>): δ [ppm] = 169.3 (s, C<sup>10</sup>), 157.0 (s, C<sup>4</sup>), 150.1 (s, C<sup>8</sup>), 140.9 (s, C<sup>3</sup>), 140.0 (s, C<sup>1</sup>), 137.4 (s, C<sup>6</sup>), 123.1 (s, C<sup>7</sup>), 121.3 (s, C<sup>9</sup>), 119.2 (s, C<sup>2</sup>), 24.9 (s, C<sup>11</sup>).

**Synthesis of *N*-Acetyl-4'-amino-2,2':6',2''-terpyridine L2. Procedure (a).** XantPhos (123 mg, 213 μmol, 9 mol %) and Pd precatalyst [Pd]<sub>2</sub> (39 mg, 53 μmol, 4.5 mol % based on Pd) were dissolved under argon in 15 mL abs. xylenes and left to stand. After 10 min 4'-chloro-2,2':6',2''-terpyridine **LB** (616 mg, 2.30 mmol, 1 equiv), acetamide (151 mg, 2.56 mmol, 1.1 equiv), and sodium *tert*-butanolate (246 mg, 2.56 mmol, 1.1 equiv) dissolved in additional 15 mL of abs. xylenes were added, and the mixture was heated to reflux for 20 h. Drying of all reagents prior to use is necessary since the resulting amide is prone to hydrolysis under the given reaction conditions in the presence of traces of water. The same workup routine as for *N*-acetyl-3,5-di(pyridin-2-yl)aniline was followed. Column chromatography on neutral Alox (Brockmann II, 3% water (w/w), solvent gradient ethyl acetate/hexanes 1:3 → 3:1) afforded pure *N*-acetyl-4'-amino-2,2':6',2''-terpyridine as off-white powder. Yield: 508 mg (1.75 mmol, 76%). Anal. Calcd C<sub>17</sub>H<sub>14</sub>N<sub>4</sub>O (290.32): C, 70.33; H, 4.86; N, 19.30. Found: C, 69.92; H, 4.81; N, 19.02%. MS(FD<sup>+</sup>): *m/z* (%) = 290.2 (100) [M]<sup>+</sup>, 313.1 (10) [M + Na]<sup>+</sup>, 603.3 (2) [2M+Na]<sup>+</sup>. <sup>1</sup>H NMR (0.5 mL of CD<sub>2</sub>Cl<sub>2</sub> + 0.1 mL of deuterated dimethyl sulfoxide): δ [ppm] = 10.23 (s, 1H, NH), 8.59 (s, 2H, H<sup>2</sup>), 8.58–8.53 (m, 2H, H<sup>8</sup>), 8.48 (d, <sup>3</sup>J<sub>HH</sub> = 8 Hz, 2H, H<sup>5</sup>), 7.76 (vtd, <sup>3</sup>J<sub>HH</sub> = 8 Hz, <sup>4</sup>J<sub>HH</sub> = 2 Hz, 2H, H<sup>6</sup>), 7.25 (ddd, <sup>3</sup>J<sub>HH</sub> = 8 Hz, 5 Hz, <sup>4</sup>J<sub>HH</sub> = 1 Hz, 2H, H<sup>7</sup>), 2.06 (s, 3H, CH<sub>3</sub>). <sup>13</sup>C{<sup>1</sup>H} NMR (CD<sub>2</sub>Cl<sub>2</sub>): δ [ppm] = 170.0 (s, C<sup>10</sup>), 156.3 (s, C<sup>4</sup>), 156.1 (s, C<sup>3</sup>), 149.0 (s, C<sup>8</sup>), 148.3 (s, C<sup>1</sup>), 137.0 (s, C<sup>6</sup>), 124.1 (s, C<sup>7</sup>), 121.0 (s, C<sup>5</sup>), 110.6 (s, C<sup>2</sup>), 24.5 (s, C<sup>11</sup>).

**Procedure (b).** To a solution of 4'-amino-2,2':6',2''-terpyridine **LC** (2.22 g, 8.94 mmol, 1 equiv) in dichloromethane (30 mL) was added a solution of acetyl chloride (10 mL, exc.) in dichloromethane (30 mL) dropwise over a period of 15 min. The resulting mixture was heated to reflux for 3 h. A slightly yellow precipitate formed during the heating. After the mixture cooled to room temperature, the solvent and the acetyl chloride were removed under reduced pressure. The remaining solid was dissolved in a mixture of water and tetrahydrofuran (1:1, 100 mL), and the pH was adjusted to 8 using aqueous sodium bicarbonate solution. The resulting colorless precipitate was collected via filtration yielding microanalytically pure *N*-acetyl-4'-amino-2,2':6',2''-terpyridine **L2** (1.09 g, 3.75 mmol). The aqueous phase was further extracted with dichloromethane (3 × 50 mL). The combined organic phases were dried over magnesium sulfate and evaporated to dryness. The crude product was purified via column chromatography on neutral Alox (Brockmann II, 3% water (w/w), solvent gradient ethyl acetate/hexanes 1:3 → 3:1) to give a second fraction of pure product as off-white solid (1.00 g, 3.44 mmol). Yield: 2.09 g (7.20 mmol, 81%). The <sup>1</sup>H NMR spectra of both fractions match those obtained from procedure a).

**Synthesis of RuCl<sub>3</sub>(R-tpy), R = COOC<sub>2</sub>H<sub>5</sub>, NHCOCH<sub>3</sub>.** A standard procedure was followed for the synthesis of the RuCl<sub>3</sub>(R-tpy) precursors.<sup>29,52</sup> Ruthenium(III) chloride hydrate (36% Ru (w/w); R = COOC<sub>2</sub>H<sub>5</sub>: 1.46 g, 5.20 mmol, 1.3 equiv; R = NHCOCH<sub>3</sub>: 566 mg, 2.01 mmol, 1.3 equiv) was dissolved in ethanol (50 mL), and the respective terpyridine (R = COOC<sub>2</sub>H<sub>5</sub>: 1.21 g, 3.96 mmol, 1 equiv; R = NHCOCH<sub>3</sub>: 450 mg, 1.55 mmol, 1 equiv) was added. The resulting mixture was heated to reflux for 3 h during which time the product precipitated as a red solid. It was filtered off and washed thoroughly with ethanol to remove residual RuCl<sub>3</sub>. The product was dried under reduced pressure and used without further purification. Yield: R =

Scheme 3. Synthetic Procedure<sup>a</sup>

<sup>a</sup>Starting from  $\text{RuCl}_3$  leading to the heteroleptic cyclometalated ruthenium complex isomers  $1(\text{PF}_6)$  and  $2(\text{PF}_6)$  as well as the amino complex  $3(\text{PF}_6)$ . Numbering for NMR assignments is included.

$\text{COOC}_2\text{H}_5$ : 1.94 g (3.78 mmol, 96%).  $\text{R} = \text{NHCOCH}_3$ : 730 mg (1.47 mmol, 95%). Because of the poor solubility of  $\text{RuCl}_3(\text{tpy-R})$  no characterization was performed.

**Synthesis of  $[\text{Ru}(\text{dpb-NHCOCH}_3)(\text{tpy-COOC}_2\text{H}_5)](\text{PF}_6)$   $1(\text{PF}_6)$ .**  $\text{RuCl}_3(\text{tpy-COOC}_2\text{H}_5)$  (100 mg, 0.195 mmol, 1 equiv) was suspended under argon in 20 mL of abs. acetone, and silver tetrafluoroborate (110 mg, 0.566 mmol, 2.9 equiv) was added. The resulting reaction mixture was heated to reflux for 2 h in the dark. After the mixture cooled to room temperature, the dark brown solution was filtered through a syringe filter to remove precipitated silver chloride prior to evaporation of the solvent. The dark, oily residue was dissolved in abs.  $n\text{BuOH}$  (20 mL), and  $\text{CH}_3\text{CONH-dpbH}$  **L1** (68 mg, 0.234 mmol, 1.2 equiv) was added. The resulting dark brown to purple solution was heated to reflux for 16 h giving an intensely colored purple solution. After removal of the solvent under reduced pressure the remaining solid was dissolved in acetonitrile (5 mL), and a solution of ammonium hexafluorophosphate (125 mg, 0.78 mmol, 4 equiv) in water (1 mL) was added. Addition of more water (~80 mL) resulted in the precipitation of the crude product, which was filtered off. Column chromatography on silica gel (solvent gradient chloroform  $\rightarrow$  chloroform/methanol 7:1, after a yellow impurity was eluted) afforded pure  $[\text{Ru}(\text{dpb-NHCOCH}_3)(\text{tpy-COOC}_2\text{H}_5)](\text{PF}_6)$  as dark purple solid. Yield: 114 mg (0.136 mmol, 70%). Anal. Calcd for  $\text{C}_{36}\text{H}_{29}\text{F}_6\text{N}_6\text{O}_3\text{PRu}$  (839.7)  $\cdot 1.5\text{H}_2\text{O}$ : C, 49.89; H, 3.72; N, 9.70. Found: C, 50.01; H, 3.50; N, 9.53%. MS( $\text{ESI}^+$ ):  $m/z$  (%) = 347.6 (1)  $[\text{M-PF}_6]^{2+}$ , 695.1 (100)  $[\text{M-PF}_6]^+$ , 1535.3 (3)  $[2\text{M-PF}_6]^+$ . HR-MS( $\text{ESI}^+$ ,  $m/z$ ): Calcd for  $\text{C}_{36}\text{H}_{29}\text{N}_6\text{O}_3\text{Ru}$   $[\text{M-PF}_6]^+$ : 695.1345; Found: 695.1336.  $^1\text{H}$  NMR ( $\text{CD}_3\text{CN}$ ):  $\delta$  [ppm] = 9.21 (s, 2H,  $\text{H}^{2\text{A}}$ ), 8.69 (s, 1H, NH), 8.57 (d,  $^3J_{\text{HH}} = 8$  Hz, 2H,  $\text{H}^{5\text{A}}$ ), 8.45 (s, 2H,  $\text{H}^{2\text{B}}$ ), 8.06 (d,  $^3J_{\text{HH}} = 8$  Hz, 2H,  $\text{H}^{5\text{B}}$ ), 7.71 (vtd,  $^3J_{\text{HH}} = 8$  Hz,  $^4J_{\text{HH}} = 1$  Hz, 2H,  $\text{H}^{6\text{A}}$ ), 7.58 (vtd,  $^3J_{\text{HH}} = 8$  Hz,  $^4J_{\text{HH}} = 1$  Hz, 2H,  $\text{H}^{6\text{B}}$ ), 7.18 (d,  $^3J_{\text{HH}} = 5$  Hz, 2H,  $\text{H}^{8\text{A}}$ ), 7.04–6.95 (m, 2H,  $\text{H}^{7\text{A}}$ ), 6.93 (d,  $^3J_{\text{HH}} = 5$  Hz, 2H,  $\text{H}^{8\text{B}}$ ), 6.58 (vt,  $^3J_{\text{HH}} = 6$  Hz, 2H,  $\text{H}^{7\text{B}}$ ), 4.63 (q,  $^3J_{\text{HH}} = 7$  Hz, 2H,  $\text{H}^{11}$ ), 2.23 (s, 3H,  $\text{H}^{14}$ ), 1.57 (t,  $J = 7$  Hz, 3H,  $\text{H}^{12}$ ).  $^{13}\text{C}\{^1\text{H}\}$  NMR

( $\text{CD}_3\text{CN}$ ):  $\delta$  [ppm] = 215.8 (s,  $\text{C}^9$ ), 169.8 (s,  $\text{C}^{13}$ ), 169.3 (s,  $\text{C}^{4\text{B}}$ ), 166.0 (s,  $\text{C}^{10}$ ), 159.8 (s,  $\text{C}^{4\text{A}}$ ), 155.2 (s,  $\text{C}^{8\text{A}}$ ), 154.3 (s,  $\text{C}^{3\text{A}}$ ), 153.1 (s,  $\text{C}^{8\text{B}}$ ), 141.9 (s,  $\text{C}^{3\text{B}}$ ), 136.9 (s,  $\text{C}^{5\text{B}}$ ), 136.2 (s,  $\text{C}^{5\text{A}}$ ), 134.4 (s,  $\text{C}^{1\text{B}}$ ), 132.5 (s,  $\text{C}^{1\text{A}}$ ), 127.6 (s,  $\text{C}^{7\text{A}}$ ), 124.8 (s,  $\text{C}^{5\text{A}}$ ), 122.9 (s,  $\text{C}^{2\text{A}}$ ), 122.6 (s,  $\text{C}^{7\text{B}}$ ), 120.8 (s,  $\text{C}^{5\text{B}}$ ), 117.9 (s,  $\text{C}^{2\text{B}}$ ), 63.3 (s,  $\text{C}^{11}$ ), 24.4 (s,  $\text{C}^{14}$ ), 14.7 (s,  $\text{C}^{12}$ ). IR (KBr disk):  $\lambda^{-1}$  [ $\text{cm}^{-1}$ ] = 3435 (crystal water), 1723 ( $\text{C}=\text{O}_{\text{ester}}$ ), 1711 ( $\text{C}=\text{O}_{\text{amide}}$ ), 1600 ( $\text{C}=\text{C}$ ), 1518 (amide II), 845 (P–F). UV–vis (MeCN):  $\lambda_{\text{max}}$  ( $\epsilon$ ) [nm ( $1 \times 10^3 \text{ M}^{-1} \text{ cm}^{-1}$ )] = 241 (49.8), 282 (62.1), 319 (29.8), 378 (14.1), 418 (shoulder, 9.7), 506 (17.3), 555 (13.7).

**Synthesis of  $[\text{Ru}(\text{dpb-COOC}_2\text{H}_5)(\text{tpy-NHCOCH}_3)](\text{PF}_6)$   $2(\text{PF}_6)$ .**  $\text{RuCl}_3(\text{tpy-NHCOCH}_3)$  (100 mg, 0.201 mmol, 1 equiv) was suspended in 20 mL of abs. acetone, and silver tetrafluoroborate (113 mg, 0.583 mmol, 2.9 equiv) was added. The resulting reaction mixture was heated to reflux for 2 h in the dark. After the mixture cooled to room temperature, the dark brown solution was filtered through a syringe filter to remove precipitated silver chloride prior to evaporation of the solvent. The dark, oily residue was dissolved in abs.  $n\text{BuOH}$  (20 mL), and  $\text{C}_2\text{H}_5\text{OOC-dpbH}$  **L3** (73 mg, 0.241 mmol, 1.2 equiv) was added. The resulting dark brown to purple solution was heated to reflux for 16 h giving an intensely colored red solution. After removal of the solvent under reduced pressure the remaining solid was dissolved in acetonitrile (5 mL), and a solution of ammonium hexafluorophosphate (130 mg, 0.80 mmol, 4 equiv) in water (1 mL) was added. Addition of more water (~80 mL) resulted in the precipitation of the crude product, which subsequently was filtered off. Column chromatography on neutral Alox (Brockmann II, 3% water (w/w), solvent gradient chloroform  $\rightarrow$  chloroform/methanol 50:1, after a yellow impurity was eluted) afforded pure  $[\text{Ru}(\text{dpb-COOC}_2\text{H}_5)(\text{tpy-NHCOCH}_3)](\text{PF}_6)$  as dark solid. Yield: 87 mg (0.104 mmol, 52%). A second fraction consisting of  $[\text{Ru}(\text{dpb-COOC}_2\text{H}_5)(\text{tpy-NH}_2)](\text{PF}_6)$  **3(PF<sub>6</sub>)** was isolated as well (40 mg, 0.050 mmol, 25%). Anal. Calcd for  $\text{C}_{36}\text{H}_{29}\text{F}_6\text{N}_6\text{O}_3\text{PRu}$  (839.7): C, 51.49; H, 3.48; N, 10.01. Found: C, 51.46; H, 3.30; N, 9.73%. MS( $\text{ESI}^+$ ):  $m/z$  (%) = 347.6 (1)

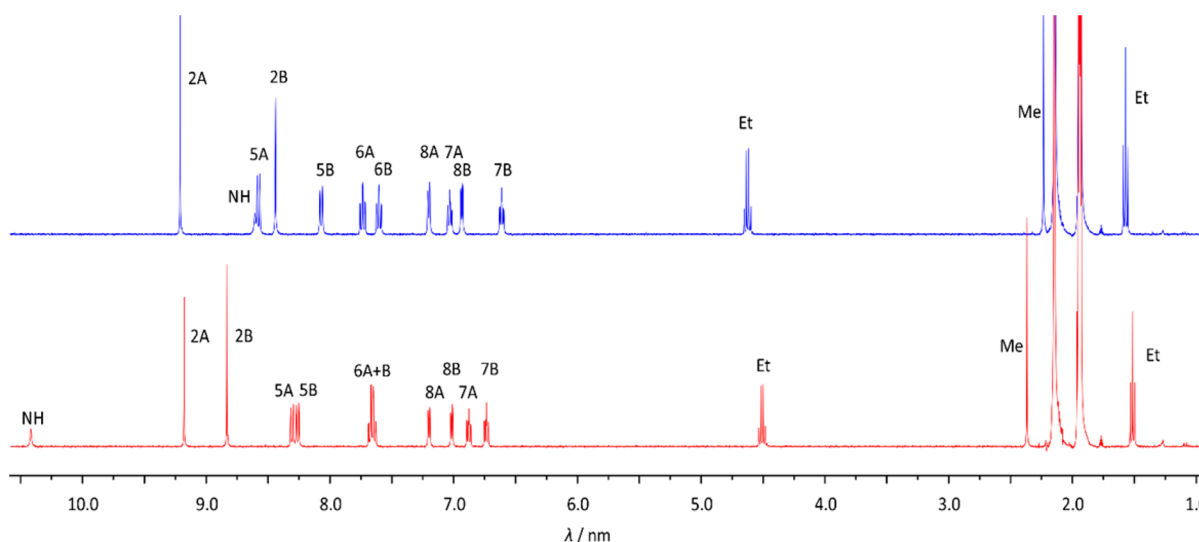


**Figure 1.**  $^1\text{H}$  NMR spectra of **1**(PF<sub>6</sub>) (upper, blue) and **2**(PF<sub>6</sub>) (lower, red) at room temperature in CD<sub>3</sub>CN (for atom numbering see Scheme 3).

[M-PF<sub>6</sub>]<sup>2+</sup>, 695.1 (100) [M-PF<sub>6</sub>]<sup>+</sup>, 1535.3 (6) [2M-PF<sub>6</sub>]<sup>+</sup>. HR-MS(ESI<sup>+</sup>, *m/z*): Calcd for C<sub>36</sub>H<sub>29</sub>N<sub>6</sub>O<sub>3</sub>Ru [M-PF<sub>6</sub>]<sup>+</sup>: 695.1345; Found: 695.1342.  $^1\text{H}$  NMR (CD<sub>3</sub>CN):  $\delta$  [ppm] = 10.42 (s, 1H, NH), 9.12 (s, 2H, H<sup>2A</sup>), 8.83 (s, 2H, H<sup>2B</sup>), 8.30 (d,  $^3J_{\text{HH}}$  = 8 Hz, 2H, H<sup>5A</sup>), 8.25 (d,  $^3J_{\text{HH}}$  = 8 Hz, 2H, H<sup>5B</sup>), 7.70–7.60 (m, 4H, H<sup>6A</sup>, H<sup>6B</sup>), 7.18 (d,  $^3J_{\text{HH}}$  = 5 Hz, 2H, H<sup>8B</sup>), 7.02 (d,  $^3J_{\text{HH}}$  = 5 Hz, 2H, H<sup>8A</sup>), 6.91–6.82 (m, 2H, H<sup>7A</sup>), 6.76–7.66 (m, 2H, H<sup>7B</sup>), 4.51 (q,  $^3J_{\text{HH}}$  = 7 Hz, 2H, H<sup>11</sup>), 2.36 (s, 3H, H<sup>14</sup>), 1.51 (t,  $^3J_{\text{HH}}$  = 7 Hz, 3H, H<sup>12</sup>).  $^{13}\text{C}\{^1\text{H}\}$  NMR (CD<sub>3</sub>CN):  $\delta$  [ppm] = 233.7 (s, C<sup>9B</sup>), 171.3 (s, C<sup>13</sup>), 169.1 (s, C<sup>4B</sup>), 168.7 (s, C<sup>10</sup>), 159.8 (s, C<sup>4A</sup>), 155.6 (s, C<sup>8A</sup>), 153.7 (s, C<sup>3A</sup>), 152.8 (s, C<sup>8B</sup>), 145.7 (s, C<sup>1A</sup>), 143.4 (s, C<sup>3B</sup>), 136.5 (s, C<sup>6A</sup>), 136.4 (s, C<sup>6B</sup>), 127.3 (s, C<sup>7A</sup>), 124.5 (s, C<sup>5A</sup>), 124.5 (s, C<sup>2B</sup>), 123.0 (s, C<sup>7B</sup>), 122.7 (s, C<sup>1B</sup>), 120.8 (s, C<sup>5B</sup>), 112.8 (s, C<sup>2A</sup>), 61.5 (s, C<sup>11</sup>), 24.9 (s, C<sup>14</sup>), 15.0 (s, C<sup>12</sup>). IR (KBr disk):  $\lambda^{-1}$  [cm<sup>-1</sup>] = 1695 (C=O<sub>ester,amide</sub>), 1600 (C=C), 1514 (amide II), 844 (P–F). UV–vis (MeCN):  $\lambda_{\text{max}}$  ( $\epsilon$ ) [nm (1  $\times$  10<sup>3</sup> M<sup>-1</sup> cm<sup>-1</sup>)] = 242 (49.2), 282 (69.4), 317 (32.4), 351 (16.9), 428 (8.7), 502 (15.2), 544 (shoulder, 11.8). (NMR and mass spectrometric data of **3**(PF<sub>6</sub>) can be found in the Supporting Information.)

## RESULTS AND DISCUSSION

**Syntheses of Ru Complexes.** Details of the ligand syntheses can be found in the Experimental Section (L1, L2) and in the Supporting Information (L3). Several different experimental protocols have been reported for the synthesis of heteroleptic ruthenium complexes with terpyridine and dipyrrolylbenzene ligands. Complexation can be performed in water/methanol solution starting from RuCl<sub>3</sub>(tpy-R) at elevated temperatures and in the presence of a tertiary amine as sacrificial reductant.<sup>41</sup> This path resembles the microwave-assisted synthesis that we employed to obtain heteroleptic bis(terpyridine)ruthenium(II) complexes in high yields.<sup>21,27</sup> For cyclometalated complexes, this procedure gives practicable yields when the coordinating carbon atom is located at one of the peripheral aromatic rings of a multidentate ligand.<sup>20,41</sup> A more robust protocol was presented in 1991 by Sauvage and co-workers in the first report on the parent cyclometalated ruthenium(II) complex [Ru(dpb)(tpy)]<sup>+</sup> (tpy = 4'-tolylterpyridine).<sup>80</sup> RuCl<sub>3</sub>(tpy) is activated via chloride abstraction with silver tetrafluoroborate. Upon addition of dpbH the desired cyclometalated complex forms readily at elevated temperatures in high yields.<sup>20,81</sup> We successfully adapted this protocol for the synthesis of the complexes presented herein (Scheme 3). Since acetylated amino groups are prone to hydrolysis and oxidation, all reactions were performed under

rigorous protective gas conditions, and only 2.9 equiv of Ag[BF<sub>4</sub>] (instead of 3.6 equiv as usually found in the literature)<sup>20,81</sup> were employed to prevent undesired side reactions. Under these conditions, we obtained the complexes **1**(PF<sub>6</sub>) and **2**(PF<sub>6</sub>) in yields of 70% and 52%, respectively, besides small quantities of a side product with a hydrolyzed acetyl amino group ([Ru(dpb-COOEt)(tpy-NH<sub>2</sub>)](PF<sub>6</sub>) **3**(PF<sub>6</sub>); see Scheme 3 and Supporting Information).

**Characterization of the Isomers.** Since both complexes **1**(PF<sub>6</sub>) and **2**(PF<sub>6</sub>) are constitutional isomers they share their elemental composition and show essentially identical mass spectra and isotope patterns (Supporting Information Figure S8). The most prominent differences are observed in the NMR spectra (Figure 1, Supporting Information Figures S9–S18). All tpy aromatic proton resonances (2A, 5A, 6A, 7A, and 8A) appear systematically further downfield in the  $^1\text{H}$  NMR spectrum (Figure 1, Scheme 3) compared to corresponding resonances of the dpb protons due to the electron-deficiency of the tpy ligand. Proton resonances of the functional groups (NHCOMe and COOEt) show the same trend. In **1**<sup>+</sup>, with the tpy-COOEt ligand, the CH<sub>2</sub> and CH<sub>3</sub> resonances of the ethyl group are found at 4.63 and 1.57 ppm, respectively, whereas in the regioisomer **2**<sup>+</sup> the corresponding protons of the dpb-COOEt ligand appear at 4.51 and 1.51 ppm, respectively. Similarly, the resonance of the acetyl CH<sub>3</sub> protons is found at 2.23 ppm in **1**<sup>+</sup> and at 2.36 ppm in **2**<sup>+</sup>, underlining the electronic influence of the different ligands. This effect is most pronounced for the amide NH proton due to its proximity to the aromatic system in both complexes. The NH resonance of tpy-NHCOMe in **2**<sup>+</sup> is found at very low field (10.42 ppm), while in **1**<sup>+</sup>, the NH resonance of dpb-NHCOMe is found at 8.69 ppm. Similar trends are also observed in the  $^{13}\text{C}$  NMR spectra (Supporting Information Figures S10 and S15). The resonance of the carbon atom C<sup>9B</sup> involved in the metal–carbon bond is found at 215.8 ppm in **1**<sup>+</sup> with the dpb-NHCOMe ligand and at 233.7 ppm in **2**<sup>+</sup> with the dpb-COOEt ligand.

Although the final complexation step requires harsh reaction conditions and long reaction times, the reaction proceeds in good yields without significant side reactions. The structural integrity of the complexes **1**<sup>+</sup> and **2**<sup>+</sup> with all functional groups is further confirmed by ESI mass spectrometry (Supporting



Information Figure S8). No significant mass peaks indicating cleavage of either the ester or the amide are detected. Interestingly, all mass spectra show a weak peak that can be assigned to  $[M-PF_6]^{2+}$  at  $m/z = 347.6$ . This is likely explained by the typically rather low oxidation potential of these electron-rich cyclometalated (polypyridine)ruthenium(II) complexes (vide infra). IR spectroscopy confirms the presence of both an ester group and a primary amide by characteristic bands for ester C=O and amide I stretching vibrations at 1723 and 1711  $cm^{-1}$  for  $1^+$  (DFT: 1733 and 1701  $cm^{-1}$ , respectively). For  $2^+$ , the IR stretching vibrations of the ester and amide carbonyl function are observed at 1697  $cm^{-1}$ . Indeed, DFT calculations predict essentially identical vibrational frequencies for both groups at  $\sim 1718$ – $1719$   $cm^{-1}$  for  $2^+$  reflecting the different electronic character of tpy and dpb (Supporting Information Figure S21). The NH deformation bands are found at  $\sim 1580$ – $1600$   $cm^{-1}$  for both isomers along with coupled C–C vibrations within the aromatic backbone (see rR spectra). The presence of the  $PF_6^-$  counterion is revealed by broad and intense P–F stretching bands at 840  $cm^{-1}$ .

**UV–vis Spectroscopic Properties of the Cyclometalated Isomers  $1^+$  and  $2^+$ .** The experimental UV–vis spectra of the two complexes  $1(PF_6)$  and  $2(PF_6)$  are depicted in Figure 2, and relevant spectroscopic data are summarized in the

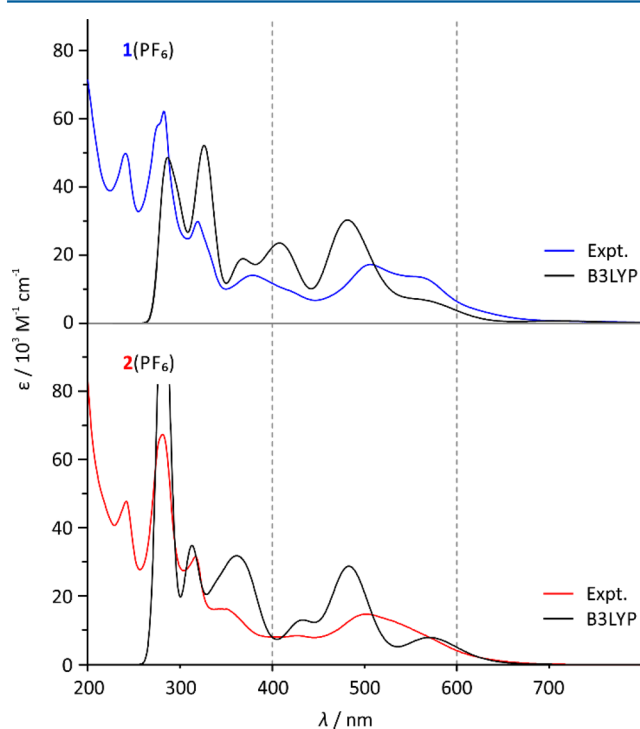


**Figure 2.** Experimental absorption spectra of  $1(PF_6)$  (upper, blue) and  $2(PF_6)$  (lower, red) in acetonitrile at room temperature;  $c = 2 \times 10^{-5}$  mol  $l^{-1}$  and calculated UV–vis spectra from TD–DFT calculations (B3LYP, black). The calculated spectra are shifted by 1000  $cm^{-1}$  to lower energies to match calculated and experimental  $\pi$ – $\pi^*$  absorption energies.

**Experimental Section.** Both complexes show absorption features of very similar shape, intensity, and energy between 200 and 325 nm. This is because of the identical ligand backbone of both complexes and is characteristic for  $[Ru-(dpb)(tpy)]^+$ -type complexes.<sup>20,81</sup> Especially the sharp absorption band at  $\sim 320$  nm with an extinction coefficient of  $\sim 3.0 \times$

$10^4$   $M^{-1} cm^{-1}$  appears to be a characteristic marker for the cyclometalation in the central position of the tridentate ligand and is well-reproduced via theoretical calculations (vide infra).

The visible region of the absorption spectra of  $1(PF_6)$  and  $2(PF_6)$  is dominated by four absorption bands (Tables 1 and 2). The strongest absorption occurs at 506 nm in  $1(PF_6)$  and at 502 nm in  $2(PF_6)$  and is best described as  $^1MLCT$  transition involving the pyridine rings of both ligands as acceptors (vide infra).<sup>20</sup> In complex  $1(PF_6)$ , the donor and acceptor effect of the respective ligand and functional group reinforce one another. An additional absorption maximum appears at the low-energy side of this  $MLCT$  transition at 555 nm. On the contrary,  $2(PF_6)$  only shows a weak shoulder in this region (Figure 2). The overall bathochromic shift of the visible light absorption features of  $1(PF_6)$  compared to  $2(PF_6)$  is accompanied by an increase in absorption intensity. Both observations are best explained by the increased push–pull effect arising from the functional groups, which lowers the highest occupied molecular orbital–lowest unoccupied molecular orbital (HOMO–LUMO) gap (cf. MO diagram, Supporting Information Figure S22) and increases the transition dipole moments for the  $^1MLCT$  transitions in  $1(PF_6)$ . In  $2(PF_6)$  on the other hand, the donor strength of dpb and the acceptor strength of tpy are both partially canceled by the substituents leading to a larger HOMO–LUMO gap and weaker  $^1MLCT$  absorptions. As a consequence,  $1(PF_6)$  appears black in the solid state and deep purple in acetonitrile solution, while  $2(PF_6)$  is dark red in the solid state and in solution. This observation is in accordance with previous results for similar complexes.<sup>20</sup>

Both compounds show two more absorption bands between 340 and 450 nm with similar intensities as the  $^1MLCT$  absorptions. In the literature the origins of these bands are consistently discussed as  $MLCT$  transitions involving the cyclometalating ligand.<sup>20,41,81</sup> However, this interpretation contradicts the observed hypsochromic shift of this absorption from 378 nm ( $1(PF_6)$ ) to 351 nm ( $2(PF_6)$ ) upon exchanging the electron-donating N-acetyl amino group for an electron-accepting carboxy group. A more consistent explanation of these absorptions is gained from TD–DFT calculations and rR experiments.

Theoretical calculations were performed using geometries optimized at the PBE/def2-SV(P) level of theory with an effective core potential at ruthenium (def2-SD, def2-TZVP). This level of theory for the geometry optimization was chosen based on data obtained by screening multiple functionals and basis sets and by comparison to geometrical parameters obtained from crystal structures of three structurally related compounds ( $[Ru(dpbc-COOMe)(tpy)](PF_6)$ ,  $[Ru(dpbc)(tpy-COOEt)](PF_6)$ , and  $[Ru(pbp-COOMe)(tpy)](PF_6)$ ).<sup>20</sup> This evaluation showed only a marginal dependence of the geometrical parameters on the size of basis set allowing for usage of a rather small and computationally efficient basis set. The variation of the structural parameters with the choice of functional was larger, but still, qualitatively similar results were obtained with all functionals under study (BP, PBE, BLYP, TPSS, TPSSH, M06L, B3LYP, PBE0). Remarkably, within the mean deviation the hybrid functionals PBE0 and B3LYP yielded identical optimized geometries compared to the corresponding GGA functionals PBE and BLYP. Hence, the more economic GGA functional PBE was preferred over hybrid functionals for geometry optimizations.

**Table 1. Spectral Decomposition of the Absorption Bands of 1(PF<sub>6</sub>) in Acetonitrile Solution in the Range from 9000 to 29 000 cm<sup>-1</sup> Using the Advanced Spectral Analysis Tool of ORCA (orca\_asa)<sup>a</sup>**

experimental data					theoretical data			
state	$\lambda^{-1}$ , cm <sup>-1</sup>	$\lambda$ , nm	$f_{\text{osc}}$	$\epsilon_{\text{max}}$ M <sup>-1</sup> cm <sup>-1</sup>	state	$\lambda^{-1}$ , cm <sup>-1</sup>	$f_{\text{osc}}$	assignment
1	12 935	773	$1.39 \times 10^{-3}$	145				Ru→tpy <sup>3</sup> MLCT
2	15 438	648	$1.15 \times 10^{-2}$	714	2	15 095	$5.5 \times 10^{-3}$	Ru→tpy <sup>1</sup> MLCT
3	16 197	617	$1.48 \times 10^{-2}$	1940				
4	17 711	565	0.102	11 300	4	18 194	0.030	Ru→tpy
					5	19 150	0.040	<sup>1</sup> MLCT
5	18 694	535	$6.99 \times 10^{-3}$	1570				
6	19 687	508	0.107	11 700	6	20 914	0.091	Ru→dpb <sup>1</sup> MLCT
7	20 910	478	0.124	6200	7	21 962	0.213	Ru→tpy
								<sup>1</sup> MLCT
8	21 399	467	$4.13 \times 10^{-3}$	690	8	21 843	$2.6 \times 10^{-3}$	Ru→dpb <sup>1</sup> MLCT
9	23 871	419	$5.38 \times 10^{-2}$	5290				
10	25 166	397	$7.88 \times 10^{-3}$	1210				
11	26 500	377	0.234	14 700				

<sup>a</sup>Eleven Gaussian bands were required to reproduce the shape of the absorption profile, and  $\lambda^{-1}$ ,  $f_{\text{osc}}$  and  $\epsilon_{\text{max}}$  are obtained from the respective fitted bands. Theoretical data are obtained from TD-DFT calculations (B3LYP) and assigned to the experimental bands based on their energy and oscillator strengths.

**Table 2. Spectral Decomposition of the Absorption Bands of 2(PF<sub>6</sub>) in Acetonitrile Solution in the Range from 9000 to 29 000 cm<sup>-1</sup> Using the Advanced Spectral Analysis Tool of ORCA (orca\_asa)<sup>a</sup>**

experimental data					theoretical data			
state	$\lambda^{-1}$ , cm <sup>-1</sup>	$\lambda$ , nm	$f_{\text{osc}}$	$\epsilon_{\text{max}}$ M <sup>-1</sup> cm <sup>-1</sup>	state	$\lambda^{-1}$ , cm <sup>-1</sup>	$f_{\text{osc}}$	assignment
1	15 479	646	$1.29 \times 10^{-3}$	208				Ru→tpy <sup>3</sup> MLCT
2	17 345	577	$1.49 \times 10^{-3}$	331	4	18 332	0.014	Ru→tpy <sup>1</sup> MLCT
3	17 455	573	$3.25 \times 10^{-2}$	2530	5	18 593	0.060	Ru→tpy <sup>1</sup> MLCT
4	19 445	514	0.216	13 000	7	21 675	0.170	Ru→dpb <sup>1</sup> MLCT
					8	21 681	0.096	
5	20 269	493	$1.54 \times 10^{-2}$	2460				
6	21 472	466	$9.72 \times 10^{-3}$	1430				
7	23 244	430	$7.42 \times 10^{-2}$	6240	11	24 120	0.111	Ru→tpy,dpb
								<sup>1</sup> MLCT
8	24 575	407	$1.39 \times 10^{-4}$	56				
9	25 035	399	$1.12 \times 10^{-2}$	1480	16	26 366	0.026	Ru→tpy <sup>1</sup> MLCT
10	28 059	356	$1.16 \times 10^{-2}$	1250				
11	29 114	343	0.504	16 300				

<sup>a</sup>Eleven Gaussian bands were required to reproduce the shape of the absorption profile, and  $\lambda^{-1}$ ,  $f_{\text{osc}}$  and  $\epsilon_{\text{max}}$  are obtained from the respective fitted bands. Theoretical data are obtained from TD-DFT calculations (B3LYP) and assigned to the experimental bands based on their energy and oscillator strengths.

Vertical excitations were generated within the TD-DFT formalism with a triple- $\xi$  basis set (def2-TZVP) and the Douglas–Kroll–Hess relativistic approximation in combination with functionals of varying Hartree–Fock (HF) exchange (PBE, 0%; TPSSh, 10%; B3LYP, 20%; PBE0, 25%). Additionally, the range-separated CAM-B3LYP functional was employed. While PBE and CAM-B3LYP both gave unsatisfactory results, TPSSh, B3LYP, and PBE0 performed equally well in TD-DFT calculations of 1(PF<sub>6</sub>) and 2(PF<sub>6</sub>) compared to the corresponding experimental data (see Supporting Information, Figures S23 and S24). A systematic increase of all transition energies and transition probabilities (oscillator strengths) was observed with increasing HF exchange (TPSSh < B3LYP < PBE0).

In the following the TD-DFT calculations using B3LYP as functional and the corresponding spectra generated with orca\_mapspc (line width 1500 cm<sup>-1</sup>) will be discussed and correlated with the experimental absorption spectra of 1(PF<sub>6</sub>) and 2(PF<sub>6</sub>). The theoretical and experimental UV–vis spectra

match reasonably well in the UV region, when the entire theoretical spectrum is shifted by 1000 cm<sup>-1</sup> to lower energies (Figure 2). In the visible region, however, the agreement is somewhat lower for both 1(PF<sub>6</sub>) and 2(PF<sub>6</sub>). This is mostly because of the weakness of TD-DFT in the description of charge transfer excitations.<sup>68,82,83</sup> Difference density plots of the 10 lowest excitations and all further significant transitions ( $f > 0.01$ ) are shown for 1<sup>+</sup> and 2<sup>+</sup> in the Supporting Information, Tables S1 and S2. In both complexes the lowest-energy transition is a well-defined HOMO–LUMO excitation with no significant admixture of other orbitals. The LUMO in both complexes is a  $\pi^*$ -orbital located at the tpy ligand, while the HOMO is essentially a  $\pi$ -orbital of the dpb ligand. The lowest-energy excitation can formally be regarded as a LL'/CT transition although ruthenium d-orbitals of the t<sub>2g</sub> set are admixed into the frontier orbitals (mixed LL'/CT and MLCT character). To differentiate between these transitions and the MLCT transitions these states will be labeled LL'/CT. Since both ligands are perpendicular to each other so are the



contributing d-orbitals, which renders the metal contribution negligible. As a consequence, these HOMO–LUMO transitions for  $1^+$  and  $2^+$  are symmetry-forbidden excitations due to the vanishing overlap integral (oscillator strengths of  $1.1 \times 10^{-5}$  and  $7.1 \times 10^{-5}$  for  $1^+$  and  $2^+$ , respectively) and do not contribute to the absorption spectrum. The corresponding  $^3\text{LL}'\text{CT}$  states, however, might play a significant role for the excited-state behavior of  $1(\text{PF}_6)$  and  $2(\text{PF}_6)$ , as discussed below.

The higher-energy excitations predicted in the visible region are  $^1\text{MLCT}$  transitions from metal d-orbitals onto the ligands. Interestingly, these excitations do not only involve tpy  $\pi^*$ -orbitals. Already in the range above 400 nm dpb accepting orbitals play a major role for the absorption profile. The UV transitions in the range between 400 and 320 nm also consist of  $^1\text{MLCT}$  transitions onto both ligands. A distinct separation of  $\text{Ru} \rightarrow \text{tpy}$  and  $\text{Ru} \rightarrow \text{dpb}$  MLCT transitions, with the former being responsible for the low-energy absorption band between 600 and 450 nm and the latter yielding the UV band between 320 and 430 nm, is not valid.

To be able to match the experimentally obtained spectrum with the theoretical data spectral decompositions of the visible range of the absorption spectra were performed. This is of particular interest considering the predicted low intensity of the  $\text{LL}'\text{CT}$  transitions in  $1(\text{PF}_6)$  and  $2(\text{PF}_6)$ . The fit data are summarized in Tables 1 and 2 for  $1(\text{PF}_6)$  and  $2(\text{PF}_6)$ , respectively. Despite the high quality of the fit (see Supporting Information, Figure S25) the low-intensity  $\text{LL}'\text{CT}$  absorptions in the low-energy edge of the absorption spectrum were not detected in either case. An upper limit of the oscillator strengths of these transitions is estimated as  $f \leq 1 \times 10^{-4}$ , which is in agreement with the computational data. The decomposition of the absorption bands supports the qualitative discussion of the spectra above. A plausible assignment of TD-DFT excitations to the most intense bands was possible based on similarities in oscillator strengths and transition energies underlining that the computational method gives a reasonable estimate of the absorption spectrum. The lowest-energy excitation observed within the spectral decomposition ( $12\,935$  and  $15\,479\text{ cm}^{-1}$  for  $1(\text{PF}_6)$  and  $2(\text{PF}_6)$ , respectively) could not be assigned to any calculated vertical singlet excitation. We ascribe these to  $^3\text{MLCT}$  absorptions that become partially spin-allowed due to spin–orbit coupling in the presence of ruthenium.<sup>4,5</sup> A complete assignment of all observed bands is of course out of reach at the presented level of theory and will generally be very difficult based on the complexity of the absorption characteristics of  $1(\text{PF}_6)$  and  $2(\text{PF}_6)$ .

**Resonance Raman Studies on  $1^+$  and  $2^+$ .** To further support this interpretation of the absorption characteristics of  $1(\text{PF}_6)$  and  $2(\text{PF}_6)$  in the visible region rR spectroscopic studies in acetonitrile solution were performed. This technique has proven to be useful just recently in the elucidation of the charge redistribution upon optical excitation in bis-(terpyridine)ruthenium(II) complexes.<sup>84,85</sup> The rR spectra of  $1(\text{PF}_6)$  and  $2(\text{PF}_6)$  with excitation at 473, 532, and 633 nm are shown in Figures 3 and 4, respectively. Since even the idealized core symmetry of these complexes ( $C_{2v}$ ) is rather low and the number of atoms is high ( $N = 76$ ), a multitude of Raman bands, many of them overlapping, is observed in the rR spectra. Qualitatively, the spectra appear very similar at the different excitation wavelengths with the only differences lying in the intensities of the bands. On one hand, the intensity of the rR

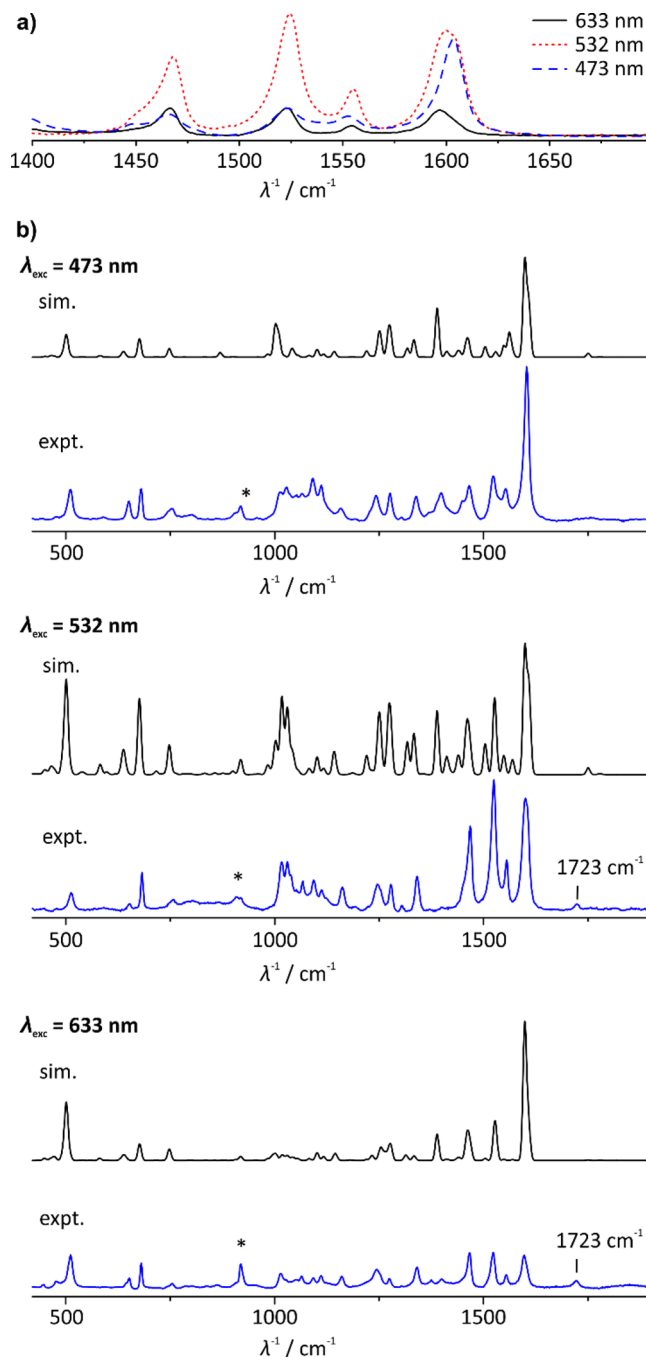


**Figure 3.** (a) Resonance Raman spectra of  $1(\text{PF}_6)$  in acetonitrile solution (298 K) in the range of 1400–1700  $\text{cm}^{-1}$  at different excitation wavelengths. (b) Experimental (blue) and DFT-calculated (black, line width = 10  $\text{cm}^{-1}$ ) rR spectra of  $1(\text{PF}_6)$  at 473, 532, and 633 nm excitation wavelength. Asterisks indicate Raman bands of  $\text{CH}_3\text{CN}$ .

spectra obviously directly depends on the extinction coefficient at the given irradiation wavelength so that a maximum in rR intensity is expected in the range of 530–470 nm for both complexes. On the other hand, the rR intensity depends on whether a given vibrational mode contributes to the geometrical reorganization associated with the given optical transition at the Franck–Condon point. Remarkably, the carbonyl stretching vibrations of both the ester and the amide functionality only play a subordinate role at all excitation wavelengths for both  $1(\text{PF}_6)$  and  $2(\text{PF}_6)$ . Since the common

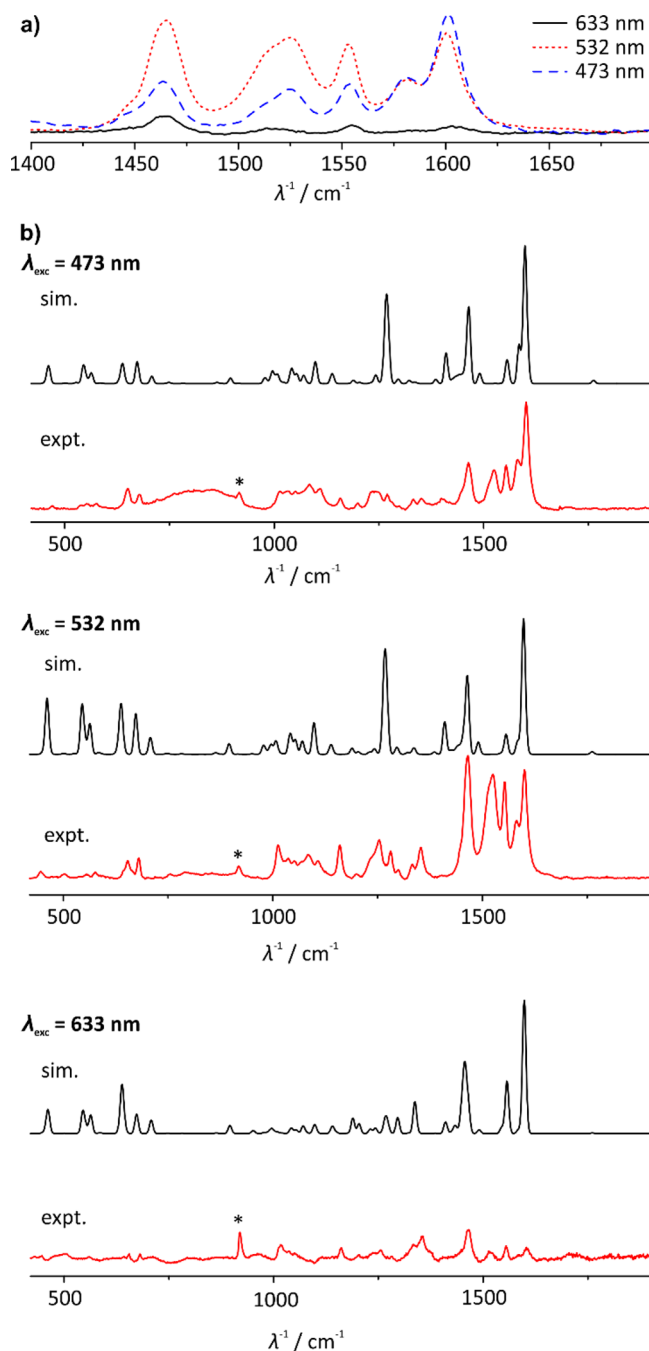


**Figure 4.** (a) Resonance Raman spectra of 2(PF<sub>6</sub>) in acetonitrile solution (298 K) in the range of 1400–1700 cm<sup>-1</sup> at different excitation wavelengths. (b) Experimental (red) and DFT-calculated (black, line width = 10 cm<sup>-1</sup>) rR spectra of 2(PF<sub>6</sub>) at 473, 532, and 633 nm excitation wavelength. Asterisks indicate Raman bands of CH<sub>3</sub>CN.

description of the intense visible range absorption band is that of a MLCT transition onto the terpyridine ligand the terpyridine ester C=O vibration at 1723 cm<sup>-1</sup> in 1(PF<sub>6</sub>) should be visible for all excitation wavelengths under study. At  $\lambda_{\text{exc}} = 633$  nm this is indeed true, but at higher energies ( $\lambda_{\text{exc}} = 532$  nm) the contribution of this vibration diminishes until disappearance at  $\lambda_{\text{exc}} = 473$  nm. At shorter wavelengths, Ru→dtp MLCT excitations become increasingly relevant for the absorption characteristics. For 2(PF<sub>6</sub>), no distinct C=O

stretching bands are observed at any excitation wavelength (cf. IR spectrum, vide supra).

Since the MLCT transitions involve  $\pi^*$ -orbitals of the aromatic ligands the corresponding CC valence vibrations should be excited and give intense rR responses (see Figures 3a and 4a). They are assigned based on DFT-calculated ground-state vibrational frequencies. The bands at 1600 cm<sup>-1</sup> for 1(PF<sub>6</sub>) and 2(PF<sub>6</sub>) are assigned to the symmetric valence vibrations (local A<sub>1</sub> symmetry) of the aromatic rings. While for 1(PF<sub>6</sub>), all these vibrations are very close in energy (DFT: between 1597 and 1605 cm<sup>-1</sup>) and overlap in the rR spectra at all excitation wavelengths, the symmetric vibration of the carboxy-substituted phenyl ring of 2(PF<sub>6</sub>) is shifted by 20 cm<sup>-1</sup> to lower energy yielding a well-resolved band in the rR spectra of 2(PF<sub>6</sub>) at 1581 cm<sup>-1</sup> (calculated at 1584 cm<sup>-1</sup>) that is not present in 1(PF<sub>6</sub>). The significant participation of the phenyl vibration in the rR spectra of 2(PF<sub>6</sub>) indicates substantial Ru→dtp character of the MLCT absorption band at 532 nm and at 473 nm. This corroborates the findings of TD-DFT calculations that Ru→dtp excitations are present even at energies below 450 nm. Since the corresponding vibration of the phenyl moiety of 1(PF<sub>6</sub>) overlaps with those of the pyridine rings a similar conclusion cannot be drawn for 1(PF<sub>6</sub>) although the width of the band suggests participation of all six totally symmetric aromatic vibrations. Similar behavior is observed for the antisymmetric (local B<sub>2</sub> symmetry) CC valence vibrations at ~1525 cm<sup>-1</sup>. While for 1(PF<sub>6</sub>) these vibrations overlap yielding one broad Raman band, a distinct shoulder at 1514 cm<sup>-1</sup> appears for 2(PF<sub>6</sub>), which is assigned to the phenyl moiety again underlining the mixed Ru→dtp/Ru→dtp MLCT character of the absorption band at 473 and 533 nm.

The intensity of the bands between 1400 and 1550 cm<sup>-1</sup> increases substantially upon increasing  $\lambda_{\text{exc}}$  from 473 to 532 nm. Ground-state vibrational frequencies and Raman intensities provide no straightforward explanation for that. The independent mode-displaced harmonic oscillator (IMDHO) model was employed, which assumes harmonic ground- and excited-state potential energy surfaces (PES) and no frequency changes upon excitation. Additionally, the excited-state PES are considered as displaced with respect to the ground-state PES along certain (or all) normal modes. More evolved theoretical approaches have been employed previously in the description of rR spectra of large molecules,<sup>86</sup> but these require much more computational time and are limited to a small number (2–3) of electronically excited states that can be considered in the calculations.

At least three prerequisites must be met to yield a qualitatively good description of the rR behavior of a given compound: First, a high quality of the normal mode displacements is crucial for a reasonable description of the rR spectra since they determine the intensity of the corresponding Raman bands. These can be computed within the above-mentioned theoretical model from excited-state gradient calculations.<sup>78,87</sup> Second, the vibrational frequencies obtained from DFT calculations must correspond well to the experimentally observed ones since these define the normal modes and have a large impact on the displacement parameters. Third, the character of the calculated electronic excited states must match that of the actual transitions. This is the most challenging part, especially for charge transfer processes, since DFT has its weakness in describing such excitations.<sup>68,82,83</sup>

All calculations were performed based on the B3LYP/def2-SVP(DKH/COSMO(acetonitrile)) optimized geometry of 1<sup>+</sup>

and  $2^+$ . Vibrational frequencies were obtained at the same level of theory. Since ORCA does not support a solvation model for excited-state gradients, the 10 lowest vertical excitations and gradients were generated in the gas phase at the B3LYP/def2-TZVP/DKH level of theory. These 10 excitations describe the spectral range under study sufficiently well. The *orca\_asa* software was then used to simulate the first-order rR spectra (higher-order Raman bands were considered but did not improve the quality of the simulations). A homogeneous line broadening of  $1200\text{ cm}^{-1}$  was assumed for all 10 excitations. The vibrational frequencies of both compounds were uniformly scaled by a factor of 0.967. This factor yields a maximum of agreement between the experimental and simulated spectra.

Neither the different MLCT optical excitations nor the molecular vibrations are energetically separated. Consequently, the rR spectrum at a given excitation wavelength is a superposition of rR profiles of the individual electronic excitations weighted by their contribution to the absorption spectrum at that wavelength. At the same time the individual Raman bands are a superposition of multiple vibrational modes. Despite the large number of approximations and assumptions the experimental rR spectra of  $1(\text{PF}_6)$  are remarkably well-reproduced by these simulations. This allows further confirmation of the character of respective absorption bands by assigning optical transitions to the respective absorption energies. The shape of the rR spectrum of  $1(\text{PF}_6)$  at 633 nm is dominated by the most intense low-energy optical transitions 4 and 5 (see Table 1 and Supporting Information Table S1), which are  $\text{Ru} \rightarrow \text{tpy}$  MLCT transitions. At  $\lambda_{\text{exc}} = 532\text{ nm}$ , the character of the involved absorptions changes and so does the rR spectrum. The range of  $1000\text{--}1300\text{ cm}^{-1}$  (in-plane deformation vibrations of the ligand backbones) is very characteristic for these changes, and a good agreement between simulation and experiment is obtained. The rR spectrum at  $\lambda_{\text{exc}} = 532\text{ nm}$  is dominated by the optical excitations 6 and 7 ( $\text{Ru} \rightarrow \text{tpy}$  and  $\text{Ru} \rightarrow \text{dpb}$ ; see Table 1 and Supporting Information Table S1). Consequently, the absorption region around the MLCT absorption maximum is composed of both  $\text{Ru} \rightarrow \text{tpy}$  and  $\text{Ru} \rightarrow \text{dpb}$  MLCT transitions. This is in contrast to the widely accepted picture of this band as exclusively arising from  $\text{Ru} \rightarrow \text{tpy}$  transitions. The quality of the rR simulation decreases somewhat at  $\lambda_{\text{exc}} = 473\text{ nm}$ . This is most likely because, at this wavelength, absorption bands of the second MLCT absorption (between 450 and 320 nm) contribute already. To keep the computational effort manageable these electronic transitions were neglected and thus are missing in the simulation. Consequently, the number of predicted rR bands is lower than experimentally observed. It is worth noting that the calculations also give an explanation for the missing resonant increase of the carbonyl stretching vibrations: For almost all major optical excitations the  $\text{C}=\text{O}$  fragment is located in a nodal plane of the involved orbitals and thus is only marginally affected by the rR effect.

$2(\text{PF}_6)$  gives a qualitatively very similar picture although the overall agreement between experiment and simulation is slightly lower (Figure 4). Especially, the  $B_2$  symmetric CC valence vibrations at  $1525\text{ cm}^{-1}$  seem to be missing in the simulation as they are calculated at higher energy at  $1556\text{ cm}^{-1}$ . At 632 nm excitation wavelength essentially off-resonance excitation is achieved leading to a spectrum with a low signal-to-noise ratio. Still, the absorption characteristics at the different wavelengths are identical. While at 632 nm low-energy MLCT transitions from ruthenium to the tpy ligand

prevail (excitations 4 and 5), the absorption at 533 nm is dominated by excitation 5 ( $\text{Ru} \rightarrow \text{tpy}$  MLCT; see Table 2 and Supporting Information Table S2). At  $\lambda_{\text{exc}} = 473\text{ nm}$   $\text{Ru} \rightarrow \text{dpb}$  transitions come into play (state 7). Again, charge transfer processes into the electron-rich dpb ligand occur at significantly lower energies than expected. In essence absorption bands between 550 and 450 nm consist of MLCT absorptions from ruthenium onto both ligands in both complexes  $1(\text{PF}_6)$  and  $2(\text{PF}_6)$ .

**Emission Properties of  $1^+$  and  $2^+$ .** Cyclometalated polypyridine complexes of ruthenium usually exhibit only weak emission. The carboxy-substituted complex  $[\text{Ru}(\text{dpb})(\text{tpy-COOR})]^+$  is nonemissive at room temperature, while its regioisomer  $[\text{Ru}(\text{dpb-COOR})(\text{tpy})]^+$  shows weak room-temperature emission.<sup>20</sup> Similarly,  $[\text{Ru}(\text{pbpy})(\text{tpy-COOR})]^+$  is nonemissive at room temperature.<sup>20</sup>

$2(\text{PF}_6)$  emits at room temperature at 751 nm with an emission quantum yield of  $1.4 \times 10^{-5}$  (Supporting Information Figure S26). At 77 K, a much more intense emission is observed with an emission maximum at 716 nm and a band shape typical for a ruthenium-based emission arising from a single vibronic progression (see Supporting Information Figure S27).<sup>27,88</sup>

The temperature dependence of the phosphorescence of  $2(\text{PF}_6)$  is shown in Figure 5. The emission intensity rapidly

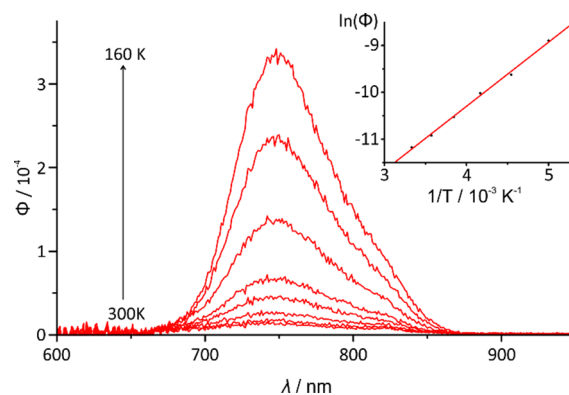


**Figure 5.** Emission quantum yield of  $2(\text{PF}_6)$  in fluid butyronitrile solution in the temperature range between 160 and 300 K (lower to upper). (inset) Plot of  $\ln(\phi)$  vs  $T^{-1}$  and the corresponding linear fit curve based on  $\ln(\phi) = \ln(k_r/k_{nr}) + \Delta E'/R \cdot 1/T$  (see text for explanation).

increases upon lowering the temperature. This behavior is easily understood following the argumentation of van Houten and Watts<sup>2</sup> and later Meyer and co-workers.<sup>3</sup> The lifetime of the emissive  $^3\text{MLCT}$  state depends on the rates of radiative and nonradiative decay,  $k_r$  and  $k_{nr}$ . Additionally, irreversible thermal depopulation of the emissive  $^3\text{MLCT}$  states via  $^3\text{MC}$  states is a relevant nonradiative relaxation pathway in (polypyridine) ruthenium complexes. Because of the irreversibility of this process it can be accounted for by a third rate constant  $k'^0$  and an Arrhenius-like activation barrier  $\Delta E'$ . As the quantum yield is proportional to the lifetime of the emissive  $^3\text{MLCT}$  state and the rate constant for radiative decay,<sup>3</sup> the following relationship between  $\phi$  and  $T$  is obtained:

$$\phi = k_r / [k_r + k_{nr} + k'^0 \cdot \exp(-\Delta E'/RT)]$$

This equation gives a nonlinear relationship between  $\ln(\phi)$  and  $T^{-1}$ , as has been shown by Meyer and co-workers.<sup>3</sup> In the



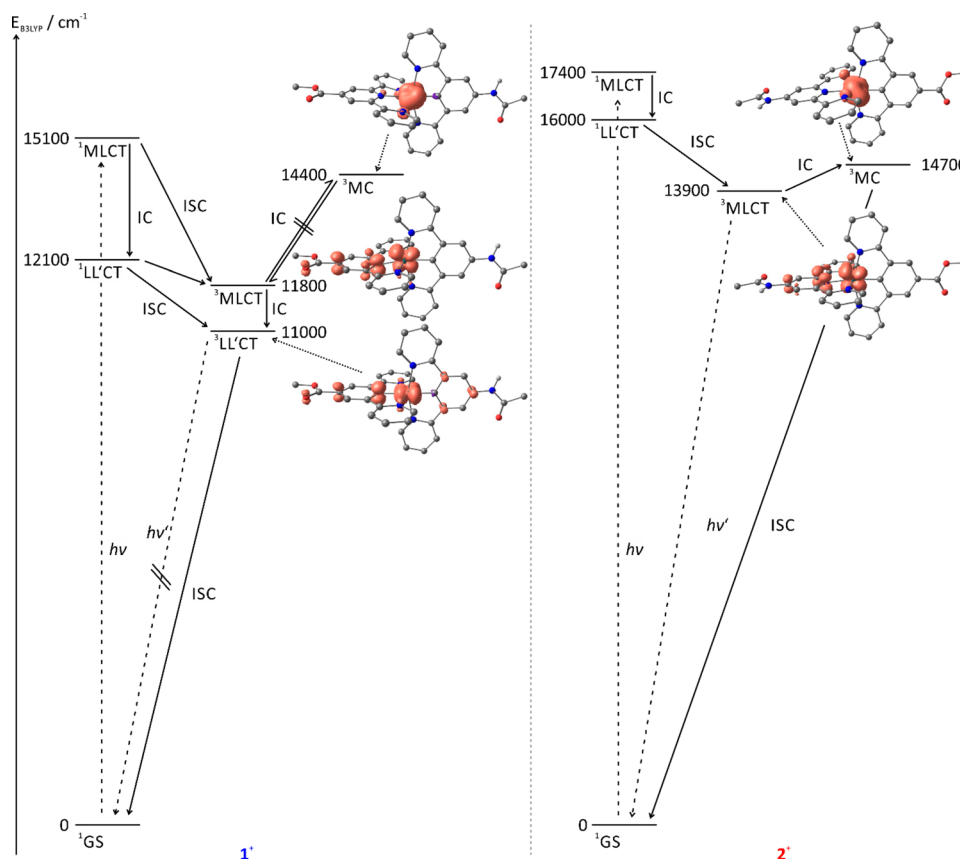


**Figure 6.** Jablonski diagrams and electronic spin densities of B3LYP-optimized triplet states of  $1^+$  and  $2^+$  (contour plots at 0.001 isosurface value).  $^1\text{MLCT}$  and  $^1\text{LL'CT}$  energies are obtained from TD-DFT calculations.  $^3\text{LL'CT}$  energy of  $1^+$  is obtained as energy difference from relaxed singlet and triplet geometries from DFT calculations. The  $^3\text{MLCT}$  energy of  $2^+$  is determined experimentally from the  $E_{00}$  emission at 77 K. Other triplet-state energies are obtained from B3LYP geometry optimizations.

present case, however (see inset of Figure 5), a linear relationship between  $\ln(\phi)$  and  $T^{-1}$  is obtained in the temperature range from 180 to 300 K. This can be explained assuming an efficient irreversible excited-state deactivation via low-lying  $^3\text{MC}$  states with a small barrier  $\Delta E'$ . With this assumption and at sufficiently high temperatures  $k_r$  and  $k_{nr}$  become negligible with respect to the exponential term associated with the rate constant  $k'^0$ , and  $\ln(\phi)$  indeed depends linearly on  $T^{-1}$ . From the linear regression, the thermal activation barrier for the  $^3\text{MLCT}$ – $^3\text{MC}$  surface crossing was determined to be  $\Delta E' = 11.4 \pm 0.5 \text{ kJ mol}^{-1}$ , which is just a fourth of the activation barrier found for  $[\text{Ru}(\text{bipy})_3]^{2+}$  ( $\Delta E' = 42.6 \text{ kJ mol}^{-1}$ ).<sup>3</sup>

To get a clearer picture of the involved excited-states, DFT calculations were performed. Using B3LYP or PBE0 as functional, one  $^3\text{MLCT}$  and one  $^3\text{MC}$  state could be localized for  $2^+$  (see Figure 6). The geometry of the  $^3\text{MLCT}$  state is essentially unaltered compared to the  $^1\text{GS}$  geometry. Because of the dipolar character of this excited state the electron-deficient ruthenium atom is slightly shifted by 3 pm toward the tpy ligand, while the dpb–tpy distance remains unaffected corresponding to a simple motion of ruthenium toward tpy in the fixed  $\text{N}_3\text{C}$  coordination sphere. A much stronger distortion with respect to the  $^1\text{GS}$  geometry is observed for the  $^3\text{MC}$  state since an antibonding metal orbital is occupied. The  $\text{Ru}-\text{N}_{\text{tpy}}$  bond lengths are substantially elongated by  $\sim 20 \text{ pm}$ , and the peripheral pyridine rings of the tpy ligand are significantly twisted out of the plane of the central pyridine ring ( $\text{N}_{\text{central}}-$

$\text{C}-\text{C}-\text{N}_{\text{peripheral}}$  dihedral angles of  $\sim 9^\circ$ ). This nicely illustrates the dissociative character of this excited state that has previously been illustrated for a series of other bis(tridentate) ruthenium complexes<sup>23</sup> and that is responsible for the intrinsic photochemical reactivity of (polypyridine)ruthenium complexes.<sup>2,3,15</sup> The  $^3\text{MC}$ – $^3\text{MLCT}$  energy difference is determined as  $9.4 \text{ kJ mol}^{-1}$  and  $19.0 \text{ kJ mol}^{-1}$  (B3LYP and PBE0, respectively). Even though this energy difference is not directly related to the experimentally determined activation barrier  $\Delta E'$  of  $11.4 \text{ kJ mol}^{-1}$  it serves as a lower limit to the latter. The calculation using B3LYP as functional seems to give a good estimate to the  $^3\text{MLCT}$ – $^3\text{MC}$  energy difference, while PBE0 slightly overestimates this energy gap.

The  $^3\text{MLCT}$ – $^3\text{MC}$  energy difference calculated for  $2^+$  is significantly lower than that obtained for  $[\text{Ru}(\text{tpy}-\text{COOH})(\text{tpy}-\text{NH}_2)]^{2+}$  at a similar level of theory ( $26.8 \text{ kJ mol}^{-1}$ ).<sup>23</sup> This might be attributed to the fact that the strong  $\sigma$ -donating effect of dpb is partially diminished by the electron-accepting ester functionality in 4-position and the tpy ligand is a weaker electron acceptor. More importantly though, cyclometalation of the central phenyl ring only raises one of the three  $^3\text{MC}$  states that are responsible for the excited-state deactivation, while the other  $^3\text{MC}$  states remain low in energy and are efficiently populated at room temperature.<sup>20</sup>

In contrast to  $2(\text{PF}_6)$ ,  $1(\text{PF}_6)$  is nonemissive both at room temperature and at 77 K. This cannot be accounted for with a thermally activated deactivation mechanism of the excited state unless the activation barrier is close to zero. Hence another

mechanism must be responsible for the excited-state deactivation. As was shown above by TD-DFT calculations, symmetry-forbidden LL'/CT transitions exist at the low-energy edge of the absorption spectra of **1**(PF<sub>6</sub>) and **2**(PF<sub>6</sub>). DFT calculations yielded a corresponding <sup>3</sup>LL'/CT excited state for **1**<sup>+</sup> (see Figure 6) as well as <sup>3</sup>MLCT and <sup>3</sup>MC states with spin distributions similar to those of **2**<sup>+</sup>. Remarkably, the complex core is essentially undistorted for the <sup>3</sup>LL'/CT state of **1**<sup>+</sup> although the Ru–C<sub>dpb</sub> bond is slightly shortened by 3 pm and the central Ru–N<sub>tpy</sub> is elongated by 6 pm corresponding to the movement of ruthenium toward the dpb ligand within a fixed ligand framework. The <sup>3</sup>MLCT state of **1**<sup>+</sup>, however, is slightly distorted compared to the <sup>1</sup>GS geometry of **1**<sup>+</sup>: The central pyridine ring of the tpy ligand is somewhat shifted out of the plane perpendicular to the dpb ligand. Again, the ruthenium atom is closer to the tpy ligand because of the dipolar character of this excited state. The dissociative character of the <sup>3</sup>MC state is also found for **1**<sup>+</sup> with characteristically elongated Ru–N<sub>tpy</sub> bond lengths and a significant distortion of the peripheral pyridine rings away from the metal center. For emissive **2**<sup>+</sup>, the <sup>3</sup>LL'/CT state could not be found. However, the corresponding <sup>1</sup>LL'/CT absorption is calculated to be ~3800 cm<sup>−1</sup> (45 kJ mol<sup>−1</sup>) higher in energy as compared to that of **1**<sup>+</sup> (Figure 6). Hence, we suggest that the <sup>3</sup>LL'/CT state does not play a significant role for the excited-state dynamics of **2**<sup>+</sup>.

The order of these three states gives a straightforward explanation to the nonemissive behavior of **1**(PF<sub>6</sub>). The lowest-lying triplet excited state is the <sup>3</sup>LL'/CT state (Figure 6). Similar to the corresponding <sup>1</sup>LL'/CT transition in the absorption (vide supra), a <sup>3</sup>LL'/CT→<sup>1</sup>GS emission process is symmetry-forbidden due to the orthogonality of the two ligands. The only available deactivation pathway is via radiationless ISC into the ground state followed by vibrational relaxation. The <sup>3</sup>MLCT state that could evolve into the ground state radiatively is ~10 kJ mol<sup>−1</sup> higher in energy than the <sup>3</sup>LL'/CT state and is only very inefficiently populated at room temperature.

Apart from the <sup>3</sup>LL'/CT state described by the strongly electron-accepting tpy and the electron-donating dpb ligand, the <sup>3</sup>MLCT–<sup>3</sup>MC separation is calculated to be substantially larger in **1**<sup>+</sup> than in **2**<sup>+</sup> also due to the stronger push–pull substitution in **1**<sup>+</sup> that stabilizes the tpy-based LUMO while at the same time destabilizing the metal-centered excited states.

In summary, the introduction of a carbon atom in the coordination sphere of ruthenium indeed increases the <sup>3</sup>MLCT–<sup>3</sup>MC energy gap sufficiently to render [Ru(dpb)(tpy)]<sup>+</sup> and **2**<sup>+</sup> emissive at room temperature, while [Ru(tpy)<sub>2</sub>]<sup>2+</sup> is silent. This effect is reinforced by attaching additional donor and acceptor functionalities in the ligand periphery that further increase this <sup>3</sup>MLCT–<sup>3</sup>MC energy gap. Unfortunately, this push–pull approach suffers from the concomitant formation of a very low-lying <sup>3</sup>LL'/CT dark state when the donor–acceptor substitution becomes too strong.

**Electrochemical Properties of 1(PF<sub>6</sub>) and 2(PF<sub>6</sub>).** The spatial orientation and symmetry of the frontier orbitals were further experimentally probed by electrochemical and EPR experiments. The cyclic voltammograms of the complexes **1**(PF<sub>6</sub>) and **2**(PF<sub>6</sub>) in acetonitrile using 0.1 M [nBu<sub>4</sub>N][PF<sub>6</sub>] as supporting electrolyte are shown in Figure 7 and Supporting Information Figures S28 and S29. Both complexes show a reversible oxidation wave at a potential of 0.02 V vs FcH/FcH<sup>+</sup> (**1**(PF<sub>6</sub>)) and 0.14 V vs FcH/FcH<sup>+</sup> (**2**(PF<sub>6</sub>)); see Table 3). Additionally, an irreversible oxidation occurs for both complexes at higher potentials. The first oxidation is ascribed

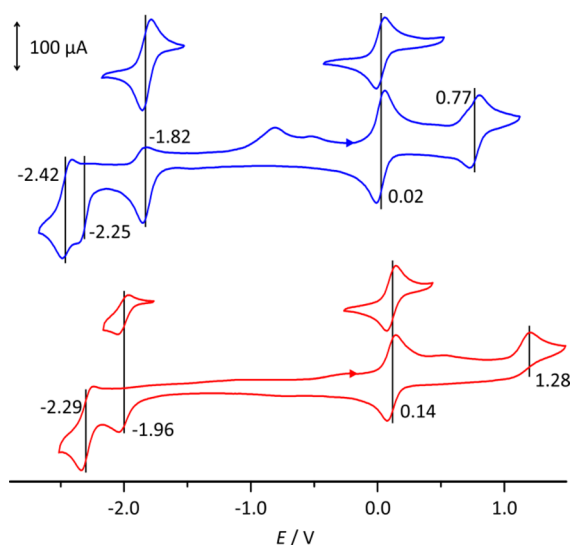


**Figure 7.** Cyclic voltammograms of **1**(PF<sub>6</sub>) (upper, blue) and **2**(PF<sub>6</sub>) (lower, red) (*c* = 1 mM) in 0.1 M acetonitrile solution of [nBu<sub>4</sub>N][PF<sub>6</sub>] at 298 K. Potentials are referenced against the FcH/FcH<sup>+</sup> couple (*E*<sub>1/2</sub> = 0.40 V vs SCE).

**Table 3. Electrochemical Data of 1<sup>+</sup>, 2<sup>+</sup>, and [(dpb)Ru(tpy)]<sup>+</sup> (1 mM) in 0.1 M [nBu<sub>4</sub>N][PF<sub>6</sub>] Electrolyte Solution<sup>a</sup>**

	<i>E</i> <sub>ox,1</sub> /V	<i>E</i> <sub>ox,2</sub> /V	<i>E</i> <sub>red,1</sub> /V	<i>E</i> <sub>red,2</sub> /V	<i>E</i> <sub>red,3</sub> /V
<b>1</b> <sup>+</sup>	0.02	0.77	−1.82	−2.25	−2.42
<b>2</b> <sup>+</sup>	0.14	1.28	−1.96	−2.29	
[Ru(dpb)(tpy)] <sup>+</sup> <sup>b</sup>	0.12	1.36	−1.95		

<sup>a</sup>Potentials are given in volts and referenced against the FcH/FcH<sup>+</sup> couple (*E*<sub>1/2</sub> = 0.40 V vs SCE). <sup>b</sup>Values taken from the literature.<sup>20</sup>

to the Ru<sup>II</sup>/Ru<sup>III</sup> redox couple with contributions from the highest occupied  $\pi$ -orbital of the cyclometalating ligand (HOMO of **1**<sup>+</sup> and **2**<sup>+</sup>, Supporting Information Figure S22) as evidenced from Mulliken spin population analysis and spin density plots of **1**<sup>2+</sup> and **2**<sup>2+</sup> (Supporting Information Figures S30 and S31). The origin of the second oxidation process, however, is less clear. DFT calculations suggest a mixed oxidation of the metal center and cyclometalating ligand as primary step (see Supporting Information Figure S32), but the irreversibility of this process points to follow-up reactions, so that the final oxidation product remains unidentified. The Ru<sup>II</sup>/Ru<sup>III</sup> oxidation is shifted by 0.6–0.7 V to lower potentials compared to bis(terpyridine)ruthenium complexes bearing the same functional groups.<sup>89</sup> This illustrates the strong  $\sigma$ -donor character of the cyclometalating ligand that greatly increases the electron density at the metal center. The NHCOMe group at the cyclometalating ligand in **1**(PF<sub>6</sub>) indeed leads to a further shift of the ruthenium-based oxidation by 0.10 V to lower values as compared to [Ru(tpy)(dpb)]<sup>+</sup>, while the COOEt substitution of the dpb ligand in **2**(PF<sub>6</sub>) slightly increases this redox potential by 0.02 V.

In the range accessible for reduction (up to −2.5 V vs FcH/FcH<sup>+</sup>) three quasireversible or irreversible redox waves are found for **1**(PF<sub>6</sub>), while for **2**(PF<sub>6</sub>) only two reduction waves are detected. These are assigned to ligand-centered reductions with the first one centered on the tpy ligand. The localization of this redox process on the ligand leads to a much stronger dependence of the corresponding redox potential on the tpy

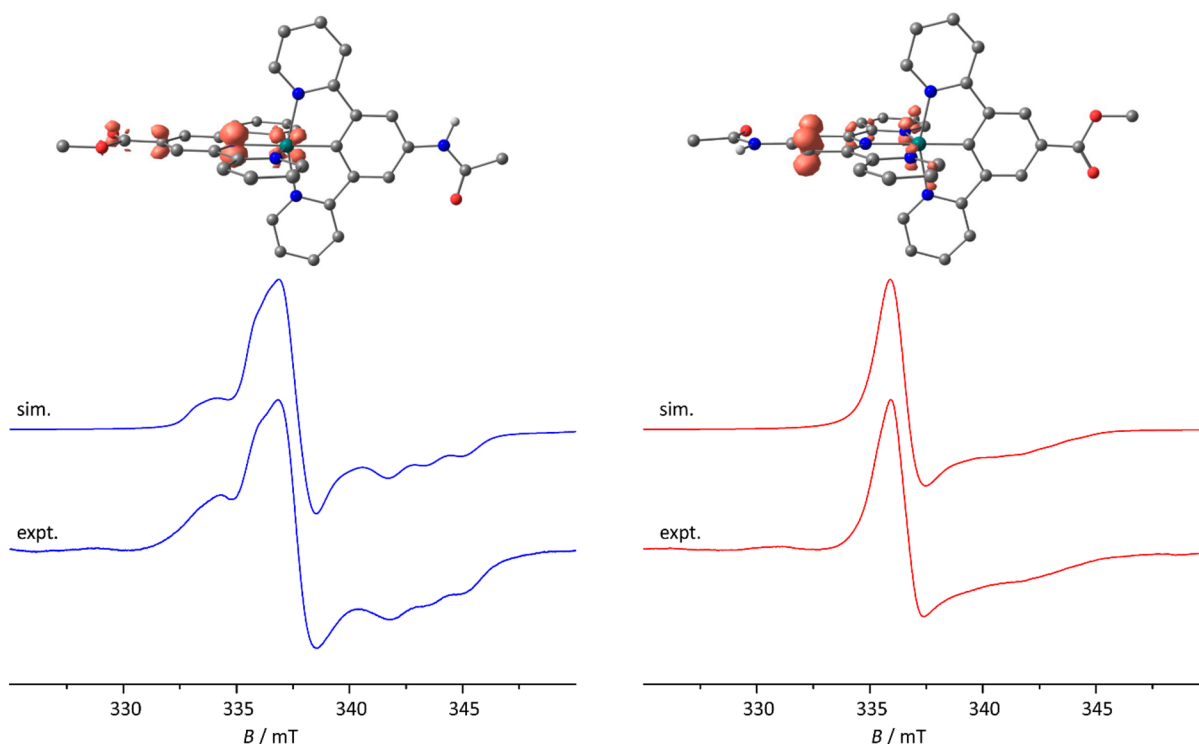


**Figure 8.** DFT-calculated spin densities (B3LYP/def2-TZVP/DKH/COSMO(acetonitrile), contour value: 0.01) of **1** (blue, left) and **2** (red, right) and experimental X-band EPR spectra ( $\nu \approx 9.4$  GHz) obtained from frozen acetonitrile solutions of **1** and **2** ( $c = 5$  mM) generated in situ with  $\text{Co}(\text{Cp}^*)_2$ . CH hydrogen atoms are omitted for clarity.

**Table 4.** Electron Paramagnetic Resonance Spectroscopic Parameters of  $1^{2+}$ ,  $2^{2+}$ , **1**, and **2** Determined Experimentally (in Frozen Acetonitrile Solution at 77 K) and Theoretically (B3LYP, def2-TZVP, DKH, COSMO(Acetonitrile))<sup>a</sup>

		$g_{1,2,3}$	$g_{\text{iso}}^b$	$\Delta g^c$	$A_{1,2,3}(^{99,101}\text{Ru})/\text{MHz}$ ( $A_{\text{iso}}/\text{MHz}$ ) <sup>d</sup>	$A_{1,2,3}(^{14}\text{N},1)/\text{MHz}$ ( $A_{\text{iso}}/\text{MHz}$ ) <sup>d</sup>	$A_{1,2,3}(^{14}\text{N},2)/\text{MHz}$ ( $A_{\text{iso}}/\text{MHz}$ ) <sup>d</sup>
$1^{2+}$	expt.	2.238, 2.176, 2.045	2.153	0.193	84, 140, 112 (112)		
	calcd.	2.312, 2.172, 2.020	2.168	0.292	88, 162, 91 (114)		
$2^{2+}$	calcd.	2.586, 2.427, 2.021	2.345	0.565	94, 187, 103 (128)		
<b>1</b>	expt.	2.0008, 1.9921, 1.9594	1.9841	0.0414	28, 36, 73 (46)	17, 10, 45 (24)	
	calcd.	2.0147, 2.0001, 1.9414	1.9854	0.0733	41, 41, 63 (48)	6, 5, 48 (19) <sup>e</sup>	
<b>2</b>	expt.	2.0008, 1.9998, 1.9685	1.9897	0.0323	8, 8, 8 (8)	3, 7, 31 (14)	3, 6, 39 (16)
	calcd.	2.0034, 2.0009, 1.9963	2.0002	0.0071	11, 8, 6 (8)	0, 0, 29 (10) <sup>f</sup>	2, 1, 46 (16) <sup>f</sup>

<sup>a</sup>For theoretically determined hyperfine coupling constants  $A(^{14}\text{N})$ , only the largest values ( $A_{\text{iso}}(^{14}\text{N}) > 10$  MHz) are given. <sup>b</sup> $g_{\text{iso}} = (g_1 + g_2 + g_3)/3$ .

<sup>c</sup> $\Delta g = g_1 - g_3$ . <sup>d</sup> $A_{\text{iso}} = (A_1 + A_2 + A_3)/3$ . <sup>e</sup>Hyperfine coupling to the central pyridine nitrogen atom of the tpy ligand. <sup>f</sup>Hyperfine coupling to one peripheral pyridine nitrogen atom of the tpy ligand.

functional groups than in the case of the metal-centered oxidation. Changing the functional group on the tpy ligand from ethyl carboxy (**1**(PF<sub>6</sub>)) to N-acetyl amino (**2**(PF<sub>6</sub>)) shifts the first reduction potential by 0.14 V to more negative values (cf. MO diagrams in Supporting Information Figure S22).

The oxidation steps in the potential range of  $-1.0$  to  $-0.5$  V for **1**(PF<sub>6</sub>) following the irreversible reduction processes are similar to those observed for bis(terpyridine)ruthenium(II) complexes bearing amide functional groups and might be associated with reduction of the NH proton at the terpyridine moiety to hydrogen.<sup>88</sup>

**Electron Paramagnetic Resonance Studies on Redox Products.** As evidenced from the cyclic voltammograms, both complexes can be oxidized to  $1^{2+}$  and  $2^{2+}$  using tris(4-bromophenyl)aminium hexachloridoantimonate as oxidant (0.67 V vs FcH/FcH<sup>+</sup> in acetonitrile, 0.70 V vs FcH/FcH<sup>+</sup> in dichloromethane) and reduced to **1** and **2** using decamethylcobaltocene  $\text{Co}(\text{Cp}^*)_2$  as reductant ( $-1.91$  V vs FcH/FcH<sup>+</sup> in

acetonitrile,  $-1.94$  V vs FcH/FcH<sup>+</sup> in dichloromethane). To study the nature of the oxidized and reduced species EPR spectra were recorded. Solutions were prepared at a 5 mM sample concentration with 0.9 equiv of the respective oxidant or reductant. While both complexes show EPR signals at 77 K after being reduced to **1** and **2** (see Figure 8), only  $1^{2+}$  is detected via X-band EPR spectroscopy at 77 K (see Supporting Information Figure S30). At room temperature in dichloromethane solution all samples were EPR-silent.

The EPR signal of  $1^{2+}$  (Supporting Information Figure S30; Table 4) is highly anisotropic ( $\Delta g = 0.193$ ) and very broad indicating a strong contribution of metal d-orbitals to the spin density. Hyperfine couplings are not resolved in the spectrum, but a good estimate of the coupling constants of the electronic spin to the nuclear spin of ruthenium ( $^{99}\text{Ru}$  and  $^{101}\text{Ru}$ :  $I = 5/2$ , natural abundance: 30%) is obtained by simulations. This coupling ( $A_{1,2,3}(^{99,101}\text{Ru}) = 84, 140, 112$  MHz) is large underlining the strong metal contribution to the radical



character. Theoretical  $g$  tensor and hyperfine coupling parameter calculations on the DFT wave function generated at the B3LYP/def2-TZVP/DKH/COSMO(acetonitrile) level of theory are in excellent agreement with the experimentally determined quantities.  $2^{2+}$  is EPR-silent at 77 K and at room temperature, but theory predicts similar  $g$  values and hyperfine coupling constants to ruthenium as observed for  $1^{2+}$  (Table 4).

EPR spectra of **1** and **2** obtained upon reduction of the respective cations (Figure 8) are substantially sharper and better-resolved. The  $g$ -value anisotropy ( $\Delta g = 0.0414$  for **1**,  $\Delta g = 0.0323$  for **2**) is reduced by a factor of 5 compared to the EPR spectrum of  $1^{2+}$  indicating a significantly stronger ligand-based character of the radical. Hyperfine couplings to the ruthenium center and one or two nitrogen atoms for **1** and **2**, respectively, are well-resolved and were determined by simulations of the experimental spectra (see Table 4). The observed spectra are easily explained with the reduction occurring at the tpy ligand (cf. MO diagram in Supporting Information Figure S22). Spin density calculations for the neutral complexes **1** and **2** explain the occurrence of a single nitrogen hyperfine coupling in **1**, while **2** shows couplings to two chemically different nitrogen atoms. The unpaired electron in **1** is essentially localized at the central pyridine ring of the tpy-COOEt ligand with its highest coefficient at the nitrogen  $p-\pi$  orbital leading to strong anisotropic superhyperfine coupling to that nitrogen nucleus, which leads to a distinctive triplet splitting of the  $g_3$  signal (Table 4). In **2**, however, the unpaired electron is delocalized over the two peripheral pyridine rings of tpy-NHCOMe in **2** with a nodal plane orthogonal to the ligand plane containing the metal center. Consequently, the EPR signal is much less well-resolved especially because the superhyperfine coupling constants to the two peripheral nitrogen nuclei differ (Figure 8). This renders unambiguous determination of all superhyperfine and hyperfine coupling constants (except  $A_3$  of the two nitrogen atoms) in **2** rather challenging, so these are estimated from line width and broadening (Table 4). The electron-donating effect of the N-acetyl amino group attached to the terpyridine ligand in **2** increases the electron density at the central pyridine ring and consequently varies the character and symmetry of the singly occupied molecular orbital (SOMO). It resembles the LUMO+1 of  $2^{2+}$  (see Supporting Information, Figure S22), whereas the SOMO of **1** is similar to the LUMO of  $1^{2+}$  (DFT: B3LYP/def2-TZVP/DKH/COSMO(acetonitrile)). The superhyperfine coupling constants to nitrogen are smaller for **2** than for **1** because of this spin delocalization over two pyridine rings (spin dilution). Furthermore, the Ru-N<sub>terminal</sub> distances are larger than the Ru-N<sub>central</sub> distances leading to a reduction of the spin-orbit coupling affecting the unpaired electron and consequently a lowering of the ruthenium hyperfine coupling in **2** and the  $g$ -value anisotropy. Since the amide bridge is rigid and rotation about the N<sub>amide</sub>-C<sub>terpyridine</sub> bond is slow at the EPR time scale (especially in rigid matrix) the spin density is asymmetric, which explains the slight differences in coupling constants to the two peripheral coordinating nitrogen atoms.

## CONCLUSION

The key properties of the cyclometalated bis(tridentate)-ruthenium(II) complexes [Ru(dpb-NHCOMe)(tpy-COOEt)]<sup>+</sup> **1**<sup>+</sup> and [Ru(dpb-COOEt)(tpy-NHCOMe)]<sup>+</sup> **2**<sup>+</sup> were revealed by introduction of electron-donating and electron-accepting functional groups in the ligand periphery of [Ru(tpy)(dpb)]<sup>+</sup> complexes. For both isomers the visible-

range absorption spectrum is dominated by MLCT transitions to the electron-poor terpyridine (Ru  $\rightarrow$  tpy) as well as the electron-rich dipyridylphenyl ligand (Ru  $\rightarrow$  dpb), which was evidenced by a combined DFT and rR spectroscopic approach. Theoretical calculations additionally suggest a symmetry-forbidden and hence experimentally undetected <sup>1</sup>LL'/CT as lowest spin-allowed optical transition in the red spectral range. The first oxidation is metal-centered in both complexes **1**(PF<sub>6</sub>) and **2**(PF<sub>6</sub>) with substantial contribution from the central phenyl ring of the dpb ligand, which corresponds to the ground state HOMO in both cases. The reduction is tpy-centered with the unpaired electron localized on the central pyridine ring in **1**(PF<sub>6</sub>), while it is delocalized over both peripheral pyridine rings of tpy in **2**(PF<sub>6</sub>). Reduction of  $2^{2+}$  to **2** reverses the order of the unoccupied orbitals LUMO and LUMO+1 as they are close in energy in  $2^{2+}$  resulting in a characteristic fingerprint in the respective EPR spectra.

While both isomers have similar absorption and electrochemical characteristics they differ fundamentally in their excited-state and emission behavior. **1**(PF<sub>6</sub>) is nonemissive both at room temperature and at 77 K, while **2**(PF<sub>6</sub>) shows a very weak emission at room temperature and a much stronger luminescence at 77 K. Temperature-dependent emission spectroscopy revealed that a very low activation barrier of ca. 11 kJ mol<sup>-1</sup> for the thermal deactivation of the emissive <sup>3</sup>MLCT state via a <sup>3</sup>MC state is responsible for the measurable, but low, emission quantum yield at room temperature.

For **1**(PF<sub>6</sub>) a completely different picture emerges. The stronger push-pull substitution substantially raises the <sup>3</sup>MC states in energy, which should lead to an increase in emission intensity compared to **2**(PF<sub>6</sub>). Indeed, DFT calculations find the <sup>3</sup>MC states high in energy. Hence, these do not contribute to the efficient excited-state deactivation in **1**(PF<sub>6</sub>). Instead, an unrecognized <sup>3</sup>LL'/CT state was found to be lower in energy than the <sup>3</sup>MLCT state in **1**(PF<sub>6</sub>). The <sup>3</sup>LL'/CT state undergoes radiationless deactivation as the radiative relaxation is symmetry-forbidden (dark state).

In essence, cyclometalation using dpb ligands shifts the <sup>3</sup>MC state above the <sup>3</sup>MLCT for **1**<sup>+</sup> compared to [Ru(tpy)<sub>2</sub>]<sup>2+</sup> thus reducing the emission quenching via thermal depopulation through <sup>3</sup>MC states. At the same time it generates low-lying <sup>3</sup>LL'/CT states that evolve radiationless into the ground state due to the symmetry-forbidden character of the transition imposed by the orthogonality of the ligands. This quenching via a <sup>3</sup>LL'/CT state is dominant for push-pull substituted cyclometalated bis(tridentate)ruthenium(II) complexes of ruthenium, and the underlying mechanisms should be transferable to iridium(III) as well,<sup>26</sup> where similar nonemissive behavior has been observed.

Despite the fact that [Ru(dpb)(tpy)]<sup>+</sup> complexes are nonemissive or only weakly emissive at room temperature, the charge-separation at the Franck-Condon point and the high reducing potential of the excited state, both induced by the cyclometalation, render these complexes promising candidates as sensitizers in photoredox applications.

## ASSOCIATED CONTENT

### Supporting Information

Experimental procedure for the synthesis of **L3**; characterization of **3**(PF<sub>6</sub>); discussion of the synthetic procedures of **L1**, **L2** and **L3**; FD mass spectra, <sup>1</sup>H and <sup>13</sup>C NMR spectra of **L1**, **L2** and **L3**; ESI mass spectra, <sup>1</sup>H, <sup>13</sup>C, COSY, HSQC, and HMBC NMR spectra of **1**(PF<sub>6</sub>) and **2**(PF<sub>6</sub>); <sup>1</sup>H and <sup>13</sup>C NMR

spectra of  $3(\text{PF}_6)$ ; solid-state IR spectra and room-temperature emission spectra of  $1(\text{PF}_6)$  and  $2(\text{PF}_6)$ ; decomposition of the absorption spectra of  $1(\text{PF}_6)$  and  $2(\text{PF}_6)$ ; MO diagrams of  $1(\text{PF}_6)$  and  $2(\text{PF}_6)$ ; TD-DFT excitations of  $1(\text{PF}_6)$  and  $2(\text{PF}_6)$  with difference density plots; cyclic and square wave voltammograms of  $1(\text{PF}_6)$  and  $2(\text{PF}_6)$ ; EPR spectrum of  $1^{2+}$ ; DFT spin-density plots of  $2^{2+}$ ,  $2^{3+}$  and  $2^{3+}$ ; Cartesian coordinates of geometry-optimized  $1^+$ ,  $1^+$ ,  $2^{2+}$ ,  $1^{2+}$ ,  $2^{2+}$ ,  $1^{3+}$ ,  $2^{3+}$ ,  $1$ , and  $2$ , as well as of the triplet states  $^3\text{LL}'\text{CT}$ ,  $^3\text{MLCT}$ , and  $^3\text{MC}$  of  $1^+$  and  $^3\text{MLCT}$  and  $^3\text{MC}$  of  $2^+$ . The Supporting Information is available free of charge on the ACS Publications website at DOI: 10.1021/acs.inorgchem.5b01151.

## AUTHOR INFORMATION

### Corresponding Author

\*Fax: +49613127277. E-mail: [katja.heinze@uni-mainz.de](mailto:katja.heinze@uni-mainz.de).

### Author Contributions

The manuscript was written through contributions of all authors; rR spectra were measured by E.E. and W.W.S. All authors have given approval to the final version of the manuscript.

### Notes

The authors declare no competing financial interest.

## ACKNOWLEDGMENTS

Parts of this research were conducted using the supercomputer Mogon and advisory services offered by Johannes Gutenberg Univ. Mainz ([www.hpc.uni-mainz.de](http://www.hpc.uni-mainz.de)), which is a member of the AHRP and the Gauss Alliance e.V. This work was financially supported by the Deutsche Forschungsgemeinschaft (GSC 266, Materials Science in Mainz, scholarship for C.K.).

## REFERENCES

- Brandt, W. W.; Dwyer, F. P.; Gyarfas, E. D. *Chem. Rev.* **1954**, *54*, 959–1017.
- van Houten, J.; Watts, R. J. *Inorg. Chem.* **1978**, *17*, 3381–3385.
- Durham, B.; Caspar, J. V.; Nagle, J. K.; Meyer, T. J. *J. Am. Chem. Soc.* **1982**, *104*, 4803–4810.
- Kalyanasundaram, K. *Coord. Chem. Rev.* **1982**, *46*, 159–244.
- Caspar, J. V.; Meyer, T. J. *J. Am. Chem. Soc.* **1983**, *105*, 5583–5590.
- Meyer, T. J. *Pure Appl. Chem.* **1986**, *58*, 1193–1206.
- Kasha, M. *Discuss. Faraday Soc.* **1950**, *9*, 14–19.
- Demas, J. N.; Taylor, D. G. *Inorg. Chem.* **1979**, *18*, 3177–3179.
- Yoon, S.; Kukura, P.; Stuart, C. M.; Mathies, R. A. *Mol. Phys.* **2006**, *104*, 1275–1282.
- Lytle, F. E.; Hercules, D. M. *J. Am. Chem. Soc.* **1969**, *91*, 253–257.
- Suzuki, K.; Kobayashi, A.; Kaneko, S.; Takehira, K.; Yoshihara, T.; Ishida, H.; Shiina, Y.; Oishi, S.; Tobita, S. *Phys. Chem. Chem. Phys.* **2009**, *11*, 9850–9860.
- Lashgari, K.; Kritikos, M.; Norrestam, R.; Norrby, T. *Acta Crystallogr., Sect. C: Cryst. Struct. Commun.* **1999**, *55*, 64–67.
- Stone, M. L.; Crosby, G. A. *Chem. Phys. Lett.* **1981**, *79*, 169–173.
- Winkler, J. R.; Netzel, T. L.; Creutz, C.; Sutin, N. *J. Am. Chem. Soc.* **1987**, *109*, 2381–2392.
- Maestri, M.; Armaroli, N.; Balzani, V.; Constable, E. C.; Thompson, A. M. W. C. *Inorg. Chem.* **1995**, *34*, 2759–2767.
- Amini, A.; Harriman, A.; Mayeux, A. *Phys. Chem. Chem. Phys.* **2004**, *6*, 1157–1164.
- Sun, P.; Krishnan, A.; Yadav, A.; Singh, S.; MacDonnell, F. M.; Armstrong, D. W. *Inorg. Chem.* **2007**, *46*, 10312–10320.
- Gong, L.; Mulcahy, S. P.; Harms, K.; Meggers, E. *J. Am. Chem. Soc.* **2009**, *131*, 9602–9603.
- Meggers, E. *Chem. - Eur. J.* **2010**, *16*, 752–758.
- Wadman, S. H.; Lutz, M.; Tooke, D. M.; Spek, A. L.; Hartl, F.; Havenith, R. W. A.; van Klink, G. P. M.; van Koten, G. *Inorg. Chem.* **2009**, *48*, 1887–1900.
- Heinze, K.; Hempel, K.; Beckmann, M. *Eur. J. Inorg. Chem.* **2006**, *2006*, 2040–2050.
- Breivogel, A.; Förster, C.; Heinze, K. *Inorg. Chem.* **2010**, *49*, 7052–7056.
- Breivogel, A.; Meister, M.; Förster, C.; Laquai, F.; Heinze, K. *Chem. - Eur. J.* **2013**, *19*, 13745–13760.
- Abrahamsson, M.; Jäger, M.; Österman, T.; Eriksson, L.; Persson, P.; Becker, H.-C.; Johansson, O.; Hammarström, L. *J. Am. Chem. Soc.* **2006**, *128*, 12616–12617.
- Schramm, F.; Meded, V.; Fliegl, H.; Fink, K.; Fuhr, O.; Qu, Z.; Kloppe, W.; Finn, S.; Keyes, T. E.; Ruben, M. *Inorg. Chem.* **2009**, *48*, 5677–5684.
- Wilkinson, A. J.; Puschmann, H.; Howard, J. A. K.; Foster, C. E.; Williams, J. A. G. *Inorg. Chem.* **2006**, *45*, 8685–8699.
- Breivogel, A.; Kreitner, C.; Heinze, K. *Eur. J. Inorg. Chem.* **2014**, *2014*, 5468–5490.
- Bolink, H. J.; Cappelli, L.; Coronado, E.; Gaviña, P. *Inorg. Chem.* **2005**, *44*, 5966–5968.
- Heinze, K.; Hempel, K.; Breivogel, A. *Z. Anorg. Allg. Chem.* **2009**, *635*, 2541–2549.
- Englman, R.; Jortner, J. *Mol. Phys.* **1970**, *18*, 145–164.
- Caspar, J. V.; Kober, E. M.; Sullivan, B. P.; Meyer, T. J. *J. Am. Chem. Soc.* **1982**, *104*, 630–632.
- Caspar, J. V.; Meyer, T. J. *J. Phys. Chem.* **1983**, *87*, 952–957.
- Parada, G. A.; Fredin, L. A.; Santoni, M.-P.; Jäger, M.; Lomoth, R.; Hammarström, L.; Johansson, O.; Persson, P.; Ott, S. *Inorg. Chem.* **2013**, *52*, 5128–5137.
- Constable, E. C.; Holmes, J. M. *J. Organomet. Chem.* **1986**, *301*, 203–208.
- Beley, M.; Collin, J. P.; Sauvage, J. P. *Inorg. Chem.* **1993**, *32*, 4539–4543.
- King, K. A.; Spellane, P. J.; Watts, R. J. *J. Am. Chem. Soc.* **1985**, *107*, 1431–1432.
- King, K. A.; Watts, R. J. *J. Am. Chem. Soc.* **1987**, *109*, 1589–1590.
- Lamansky, S.; Djurovich, P.; Murphy, D.; Abdel-Razzaq, F.; Lee, H.-E.; Adachi, C.; Burrows, P. E.; Forrest, S. R.; Thompson, M. E. *J. Am. Chem. Soc.* **2001**, *123*, 4304–4312.
- Lowry, M. S.; Bernhard, S. *Chem. - Eur. J.* **2006**, *12*, 7970–7977.
- Constable, E. C.; Housecroft, C. E. *Polyhedron* **1990**, *9*, 1939–1947.
- Bomben, P. G.; Robson, K. C. D.; Sedach, P. A.; Berlinguette, C. P. *Inorg. Chem.* **2009**, *48*, 9631–9643.
- Bomben, P. G.; Koivisto, B. D.; Berlinguette, C. P. *Inorg. Chem.* **2010**, *49*, 4960–4971.
- Chirdon, D. N.; McCusker, C. E.; Castellano, F. N.; Bernhard, S. *Inorg. Chem.* **2013**, *52*, 8795–8804.
- Colombo, M. G.; Hauser, A.; Gudel, H. U. *Inorg. Chem.* **1993**, *32*, 3088–3092.
- Hay, P. J. *J. Phys. Chem. A* **2002**, *106*, 1634–1641.
- Flamigni, L.; Barbieri, A.; Sabatini, C.; Ventura, B.; Barigelli, F. *Top. Curr. Chem.* **2007**, *281*, 143–203.
- Wadman, S. H.; Kroon, J. M.; Bakker, K.; Lutz, M.; Spek, A. L.; van Klink, G. P. M.; van Koten, G. *Chem. Commun.* **2007**, 1907–1909.
- Wadman, S. H.; Kroon, J. M.; Bakker, K.; Havenith, R. W. A.; van Klink, G. P. M.; van Koten, G. *Organometallics* **2010**, *29*, 1569–1579.
- Bruno, N. C.; Tudge, M. T.; Buchwald, S. L. *Chem. Sci.* **2013**, *4*, 916–920.
- Chavarot, M.; Pikramenou, Z. *Tetrahedron Lett.* **1999**, *40*, 6865–6868.
- Constable, E. C.; Ward, M. D. *J. Chem. Soc., Dalton Trans.* **1990**, 1405–1409.
- Fallahpour, R.-A. *Eur. J. Inorg. Chem.* **1998**, *1998*, 1205–1207.
- Suda, K.; Akagi, K. *Macromolecules* **2011**, *44*, 9473–9488.

- (54) Fulmer, G. R.; Miller, A. J. M.; Sherden, N. H.; Gottlieb, H. E.; Nudelman, A.; Stoltz, B. M.; Bercaw, J. E.; Goldberg, K. I. *Organometallics* **2010**, *29*, 2176–2179.
- (55) Connelly, N. G.; Geiger, W. E. *Chem. Rev.* **1996**, *96*, 877–910.
- (56) Stoll, S.; Schweiger, A. *J. Magn. Reson.* **2006**, *178*, 42–55.
- (57) Neese, F. *WIREs Comput. Mol. Sci.* **2012**, *2*, 73–78.
- (58) Neese, F.; Wennmohs, F.; Hansen, A.; Becker, U. *Chem. Phys.* **2009**, *356*, 98–109.
- (59) Izsák, R.; Neese, F. *J. Chem. Phys.* **2011**, *135*, 144105.
- (60) Perdew, J. P.; Burke, K.; Ernzerhof, M. *Phys. Rev. Lett.* **1996**, *77*, 3865–3868.
- (61) Perdew, J. P.; Burke, K.; Ernzerhof, M. *Phys. Rev. Lett.* **1997**, *78*, 1396.
- (62) Schäfer, A.; Horn, H.; Ahlrichs, R. *J. Chem. Phys.* **1992**, *97*, 2571–2577.
- (63) Schäfer, A.; Huber, C.; Ahlrichs, R. *J. Chem. Phys.* **1994**, *100*, 5829–5835.
- (64) Andrae, D.; Häußermann, U.; Dolg, M.; Stoll, H.; Preuß, H. *Theoret. Chim. Acta* **1990**, *77*, 123–141.
- (65) Weigend, F.; Ahlrichs, R. *Phys. Chem. Chem. Phys.* **2005**, *7*, 3297–3305.
- (66) Sinnecker, S.; Rajendran, A.; Klamt, A.; Diedenhofen, M.; Neese, F. *J. Phys. Chem. A* **2006**, *110*, 2235–2245.
- (67) Vlček, A.; Zális, S. *Coord. Chem. Rev.* **2007**, *251*, 258–287.
- (68) Magyar, R. J.; Tretiak, S. *J. Chem. Theory Comput.* **2007**, *3*, 976–987.
- (69) Tao, J.; Perdew, J. P.; Staroverov, V. N.; Scuseria, G. E. *Phys. Rev. Lett.* **2003**, *91*, 146401.
- (70) Becke, A. D. *J. Chem. Phys.* **1993**, *98*, 5648–5652.
- (71) Adamo, C.; Barone, V. *J. Chem. Phys.* **1999**, *110*, 6158–6170.
- (72) Yanai, T.; Tew, D. P.; Handy, N. C. *Chem. Phys. Lett.* **2004**, *393*, 51–57.
- (73) Douglas, M.; Kroll, N. M. *Ann. Phys.* **1974**, *82*, 89–155.
- (74) Hess, B. *Phys. Rev. A: At., Mol., Opt. Phys.* **1985**, *32*, 756–763.
- (75) Hess, B. *Phys. Rev. A: At., Mol., Opt. Phys.* **1986**, *33*, 3742–3748.
- (76) Jansen, G.; Hess, B. *Phys. Rev. A: At., Mol., Opt. Phys.* **1989**, *39*, 6016–6017.
- (77) Pantazis, D. A.; Chen, X.-Y.; Landis, C. R.; Neese, F. *J. Chem. Theory Comput.* **2008**, *4*, 908–919.
- (78) Petrenko, T.; Neese, F. *J. Chem. Phys.* **2007**, *127*, 164319.
- (79) Petrenko, T.; Neese, F. *J. Chem. Phys.* **2012**, *137*, 234107.
- (80) Beley, M.; Collin, J. P.; Louis, R.; Metz, B.; Sauvage, J. P. *J. Am. Chem. Soc.* **1991**, *113*, 8521–8522.
- (81) Koivisto, B. D.; Robson, K. C. D.; Berlinguette, C. P. *Inorg. Chem.* **2009**, *48*, 9644–9652.
- (82) Dreuw, A.; Weisman, J. L.; Head-Gordon, M. *J. Chem. Phys.* **2003**, *119*, 2943.
- (83) Tozer, D. J. *J. Chem. Phys.* **2003**, *119*, 12697–12699.
- (84) Heinze, K.; Hempel, K.; Tschierlei, S.; Schmitt, M.; Popp, J.; Rau, S. *Eur. J. Inorg. Chem.* **2009**, *2009*, 3119–3126.
- (85) Preiß, J.; Jäger, M.; Rau, S.; Dietzek, B.; Popp, J.; Martínez, T.; Presselt, M. *ChemPhysChem* **2015**, *16*, 1395–1404.
- (86) Egidi, F.; Bloino, J.; Cappelli, C.; Barone, V. *J. Chem. Theory Comput.* **2014**, *10*, 346–363.
- (87) Heller, E. J.; Sundberg, R.; Tannor, D. J. *Phys. Chem.* **1982**, *86*, 1822–1833.
- (88) Kreitner, C.; Grabolle, M.; Resch-Genger, U.; Heinze, K. *Inorg. Chem.* **2014**, *53*, 12947–12961.
- (89) Breivogel, A.; Hempel, K.; Heinze, K. *Inorg. Chim. Acta* **2011**, *374*, 152–162.